POLITECNICO DI TORINO

Facoltà di Ingegneria

Master degree in Mechatronic Engineering

Master Thesis

FlegX

Characterization and Control of a Flexible Robotic Leg

Advisor
Prof. Alessandro Rizzo

Company supervisor
Ferdinando Cannella, Ph.D.

Candidate
Francesco Bonicelli

December 2018

Acknowledgements

Once the end of my university career has arrived, it is time to thank all those who have made this experience less difficult. But first I would like to say that it was an honour for me to have done my thesis work at the Italian Institute of Technology, since as a child I was fascinated by the research carried out by this centre in the field of robotics.

The first thanks goes to the prof. Rizzo for his impeccable availability and professionalism, which has given me invaluable help, ever since I received the thesis proposal from the IIT, both from the bureaucratic point of view and in the writing of the thesis.
A big thank you also goes to Dr. Cannella, who has been able to show me how to interface with the world of research with great passion and dedication. In addition, he has always been available to give me advice on how to deal with difficulties and do my job better.
My deepest gratitude goes to Dr. Daniele Ludovico, who has driven me since my first days at the IIT until the conclusion of the thesis. His patience in answering all my doubts or advising me on the path to be taken in cases of difficulty has made sure that I never lose hope, even in the most difficult moments.
Thanks in general to all those who welcomed me at IIT with great joy and sympathy and made my stay at the institute unforgettable.
I have to thank Dr. Cristiano Pizzamiglio for his collaboration and his remote support.

At this point I think I have to thank not only those who have been close to me during these last months during the development of the thesis, but above all those who have been with me for a longer time, until this important milestone has been reached.
I start by thanking my brother Stefano, who has supported and stand me his whole life.
Another thanks is for my parents and my family in general, who has always let me follow my interests and has always supported me in my choices, both morally and economically.
Finally, I have to thank all the friends who had this adventure called university with me, with whom I spent moments of happiness and moments of despair, but that anyway never left me.
Among friends a special thanks goes to Vito, who lived all the university period with me, both in moments of confrontation and in those of fun.
The last thanks goes to myself, that I had the strength and the constancy of always going forward, so as to reach this important goal of my life.

Giunto il termine della mia carriera universitaria è arrivato il momento di ringraziare tutti coloro che hanno reso questo cammino meno difficoltoso. Prima però ci tengo a dire che per me è stato un onore aver svolto il lavoro di tesi presso l'Istituto Italiano di Tecnologia, in quanto fin da piccolo son rimasto affascinato dalle ricerche svolte da tale centro nell'ambito della robotica.

Il primo ringraziamento va al prof. Rizzo per la sua impeccabile disponibilità e professionalità, il quale mi ha dato un aiuto inestimabile, sin da quando ho ricevuto la proposta di tesi da parte dell'IIT, sia dal punto di vista burocratico che nella stesura della tesi.
Un sentito ringraziamento va anche al dott. Cannella, il quale ha saputo mostrarmi come interfacciarsi al mondo della ricerca con grande passione e dedizione. Inoltre, è sempre stato disponibile a darmi consigli su come affrontare le difficoltà e svolgere il mio lavoro al meglio.
La mia più profonda gratitudine va al dott. Daniele Ludovico, il quale mi ha accompagnato sin dai miei primi giorni presso l'IIT fino alla conclusione della tesi. La sua pazienza nel rispondere ad ogni mio dubbio o nel consigliarmi la strada da intraprendere nei casi di difficoltà ha fatto sì che non perdessi mai la speranza, anche nei momenti più difficili.
Un ringraziamento è rivolto in generale a tutti coloro che presso l'IIT mi hanno accolto con grande gioia e simpatia e hanno reso la mia permanenza presso l'istituto indimenticabile.
Non posso non ringraziare il dott. Cristiano Pizzamiglio per la sua collaborazione e il suo supporto da remoto.

A questo punto ritengo che sia doveroso ringraziare non soltanto coloro che mi sono stati vicini durante questi ultimi mesi durante lo sviluppo della tesi, ma soprattutto chi mi ha accompagnato da più tempo, fino al raggiungimento di questo importante traguardo.
Inizio ringraziando mio fratello Stefano, il quale mi sopporta e supporta da tutta la sua vita.
Un altro ringraziamento è rivolto ai miei genitori e alla mia famiglia in generale, la quale mi ha sempre lasciato seguire i miei interessi e mi ha sempre supportato nelle mie scelte, sia moralmente che economicamente.
Infine, è doveroso ringraziare tutti gli amici che mi hanno accompagnato in questa avventura chiamata università, con i quali ho passato momenti di felicità e momenti di sconforto, ma che comunque andassero le cose non mi hanno mai abbandonato.
Tra gli amici un ringraziamento speciale va a Vito, il quale mi ha accompagnato per tutto il periodo universitario, sia nei momenti di confronto che in quelli di svago.
L'ultimo ringraziamento va a me stesso, che ho avuto la forza e la costanza di andare sempre avanti, così da raggiungere questo importante traguardo della mia vita.

Contents

List of Figures

List of Tables

Abstract

The purpose of this Master Thesis is to a study the effects induced by structural elasticity in robotic systems.

New challenges are oriented towards bioinspired, safe and energy-efficient solutions. For instance, nowadays advanced robots are not confined anymore to factories and manufacturing tasks; rather, they are designed to help humans in a vast variety of daily tasks. The introduction of elastic components may constitute a viable solution. Robots conceived as structurally flexible become lighter, this means that they need less energy consumption to perform the same tasks with respect to their rigid counterparts. In addiction elastic components can store energy and release it in a later time, leading to an increase of the efficiency of the whole system. Furthermore, flexible components can be a solution to problems induced by the interaction with unstructured environment, because they can handle impulsive forces caused by both desired and/or accidental contact with either the surroundings or objects.

To reach this achievement a test rig has been used composed by an already-made two links robotic leg with one of them conceived as flexible. Then, the goal of this work is to design a suitable controller for its actuation as a first step in designing a new concept of a jumping humanoid robot as well as industrial robots. First an accurate characterization of the prototype is made in order to either measure or estimate all its electro-mechanical properties. Experimental results are compared to the simulations performed during the mechanical design phase. Afterwards the leg mathematical model is derived through the bond graph approach for both the flight and the stance phases. Once planned the closed loop system the friction disturbance effect is examined, then a controller for each phase is designed through the loop shaping technique and experimentally tuned.
Finally, the achieved results are discussed along with the prototype structural, electronic and computer problems and limitations and future improvements are proposed.

Chapter 1

Introduction

Robots are artificial devices designed to perform different tasks, typically devoted to the man's assistance or, in some cases, its replacements. Some examples are the manufacture, construction, handling of heavy and hazardous materials, or in prohibitive environments or non-compatible with the human condition ones.
The first robots were used for simple tasks as transfer objects from one point to another, since they had no external sensing. The first industrial robot industry born in 1956 from the meeting of George Devol, who two years earlier had written a patent on a machine called a Programmed Transfer Article, and Joseph Engelberger. The company, called Unimation, installed the first robot in General Motor's (GM) factory in Trenton to serve a die casting machine. [1]
Those robots replaced humans in monotonous, repetitive, heavy and dangerous tasks. When the robots could manage both a more complex motion, but also had external sensor capacity, more complex applications followed, like welding, grinding, deburring and assembly. Nowadays advanced robots are not confined anymore to factories and manufacturing tasks, they are spreading into the medical, agricultural, exploration, maintenance and assistance fields.

Up to now, most of the robots are designed totally rigid, this allows them to be moved at high speed with high precision and repeatability. However, rigid bodies are necessary big and, above all, heavy. This means that to reach high performances those robots require an high energy consumption. Moreover, if those robots have to interact with people, they have to be moved very slowly in order to avoid injuring someone. This leads to a strong reduction of their performance possibilities.
The introduction of elastic components in the robots structure may constitute a viable solution. If the deformations are taken into account during the mechanical design phase, it is possible to choose smaller components, resulting in a lightening of the structure. In addiction, elastic components can store energy and release it in a later time. Furthermore, it is possible to amplify the actuators effort by exploiting the resonance phenomenon. These brings to an increase of the hole system efficiency and to an improve of their performance in terms of energy consumption. In addiction, an elastic structure is able to absorb part of the shock produced by the robot interaction with both desired and/or accidental contact with either the surroundings or objects. This makes the interaction with both people and unstructured environment safer avoiding damaging both the robot and the surroundings.

Among all the robot categories, legged robots are particular interesting thanks to their

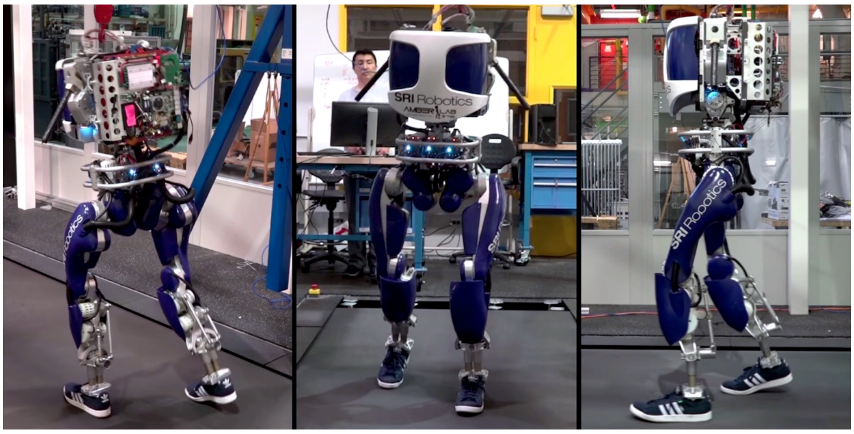

Figure 1.1: Durus robot, image: AMBER Lab/Georgia Tech

ability to move on uneven terrains with respect to wheeled ones.
One of the difficulties in the legged robot control is the transition management between the two phases, flight and stance. Legged robots can be modelled following the hybrid system theory, in particular it is necessary to derive different models for describing the leg dynamics either standing on the ground or lifted. The transition between the two models introduces a discontinuity into the system states, this can leads to instability. Moreover, from the mechanical point of view, the impulsive forces generated from the impact of the leg with the ground can damage the structural components.
The introduction of flexible elements can reduce the discontinuity introduced by the impact with the ground since its deformation smooths the impulsive torques transmitted to the joints. This filtering action brings benefits also to the structure since, reducing the strain to witch it is subject, its integrity is preserved.
Last the introduction of flexible structural elements allows the robot to store energy without adding further components, letting the structure as light as possible and increasing the overall efficiency of the system.

In the last years, thanks to the advent of high-performance computers, the development of flexible robotic structures arose. Focusing on bipedal robots, it is possible to date several examples of both academic and commercial robots that has some kind of elasticity.
The elasticity has been studied for years, starting from the Series Elastic Actuation. Some application examples are Spring Flamingo [2], KURMET Bipedal Robot [3], Hume robot [4] and also from the IIT with iCub [5, 6].
The humanoid robot DURUS [7], shown in Figure 1.1, revealed to the public at the DARPA Robotics Challenge (DRC) in June 2015, uses passive springs in the ankles in order to damp the shocks and to save energy. The main key of this research is to analyze the walk efficiency.
A different approach has been followed by the Festo company and by the Korea Advanced Institute of Science and Technology (KAIST). They designed respectively Bionickangaroo the first and Raptor robot the second with elastic tendons aimed to save energy during their movements. The two robots are shon in Figure in Figure 1.2. Bionickangaroo is able to emulate the jumping behaviour of real kangaroos, which means that it can efficiently recover energy from one jump to help it make the successive one. It is able to jump 40 cm vertically and 80 cm horizontally. Raptor robot [8] is a sprinting robot with two nimble legs and a mechanism that mimics a tail. It is able to reach a speed of 46 km/h on a

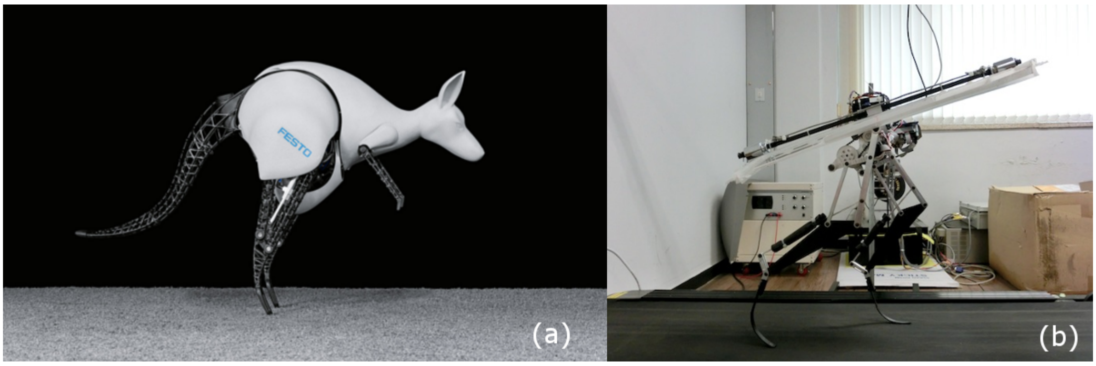

Figure 1.2: (a): Bionickangaroo by Festo, image: www.festo.com; (b): Raptor robot by KAIST, image: KAIST Mechatronics, Systems, and Control Lab

treadmill.
Another project is called Salto-1P [9], a jumping robot able to perform a standing vertical leap of $1.25m$. This result has been achieved thanks to the introduction of a torsional spring that makes the dynamics of the robot like a "spring-loaded inverted pendulum". Salto-1P is shown in Figure 1.3.
Despite the high dynamic performances and the complex architecture of the aforementioned robots, none of the cited examples has a flexible structure.
Flexible links in bipedal robots are first introduced in Athlete Robot [10], a bipedal robot that runs on legs powered by pneumatic muscles. Athlete uses air-motors that mimic human muscles in order to study 'artificial' muscle-skeletal system for the robot. The flexible lower-legs are composed by prosthetic blades, of the type that double amputees use to run.

To deepen the effects induced by the structural elasticity in robotic systems, the Italian Institute of Technology (IIT) started a project called FlegX (FLEXible LEG) as a first step in the design of a jumping humanoid robot with flexible limbs.
In the end of the 2017 the first prototype was built, this is fully described in chapter 2. The aim of this Thesis is to validate the extended numerical simulation campaign carried out during the mechanical design phase. In order to achieve this result, it is necessary to analyze the physical system and to design a suitable controller for its actuation.
In the first part of this work an accurate characterization of the prototype is made in order to either measure or estimate all its electro-mechanical properties. The main goal

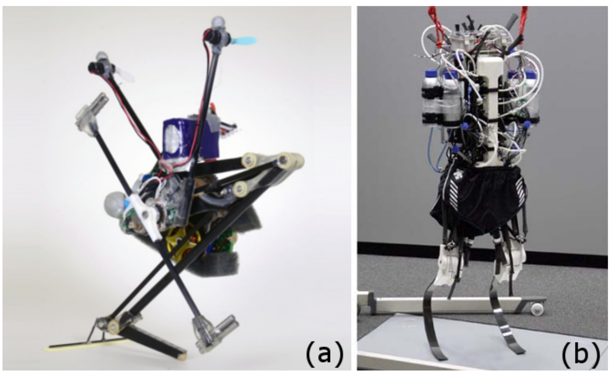

Figure 1.3: (a): Salto-1P robot, image: Biomimetic Millisystems Lab/UC Berkeley; (b) Athlete Robot, image: http://www.isi.imi.i.u-tokyo.ac.jp

of this process is to acquire all the data necessary for the computation of a model of the leg that can be used during the control design phase. To study the strain gauge, three different methods are proposed: the Least Squares approach for the output error model, the Linear Programming one for the output error model in the Set Membership Identification framework, and the Polynomial Optimization Problem for the error in variable model. Further, the dynamical properties of the flexible link are analyzed through the Fourier analysis of its impulse response. The two torque sensors are characterised through the Least Squares approach. After, the mechanical properties like masses, inertias around the two revolute joints and bearings friction are either measured or estimated through the physical pendulum approach.
Once all the needed electro-mechanical properties are computed, a mathematical model of the leg is derived through the Bond-Graph modelling technique. Describing the dynamics of the leg through an hybrid dynamic system model, it is necessary to compute four different models, one for each actuated subsystem in each jump configuration (flight or stance). In order to derive the closed loop model for the control design phase, the motor model is derived through system identification.
Finally, four different controllers, one for each derived model, are designed. The proposed controller is based on a phase-lead network with a feed-forward term used to compensate the gravity effect.

Chapter 2

Prototype description

FlegX is a novel robotic mechanism whose main characteristic is to have one link flexible. The actual configuration shown in Figure 2.1 comes from an extended numerical simulation campaign carried out during the design process described in [12, 13].

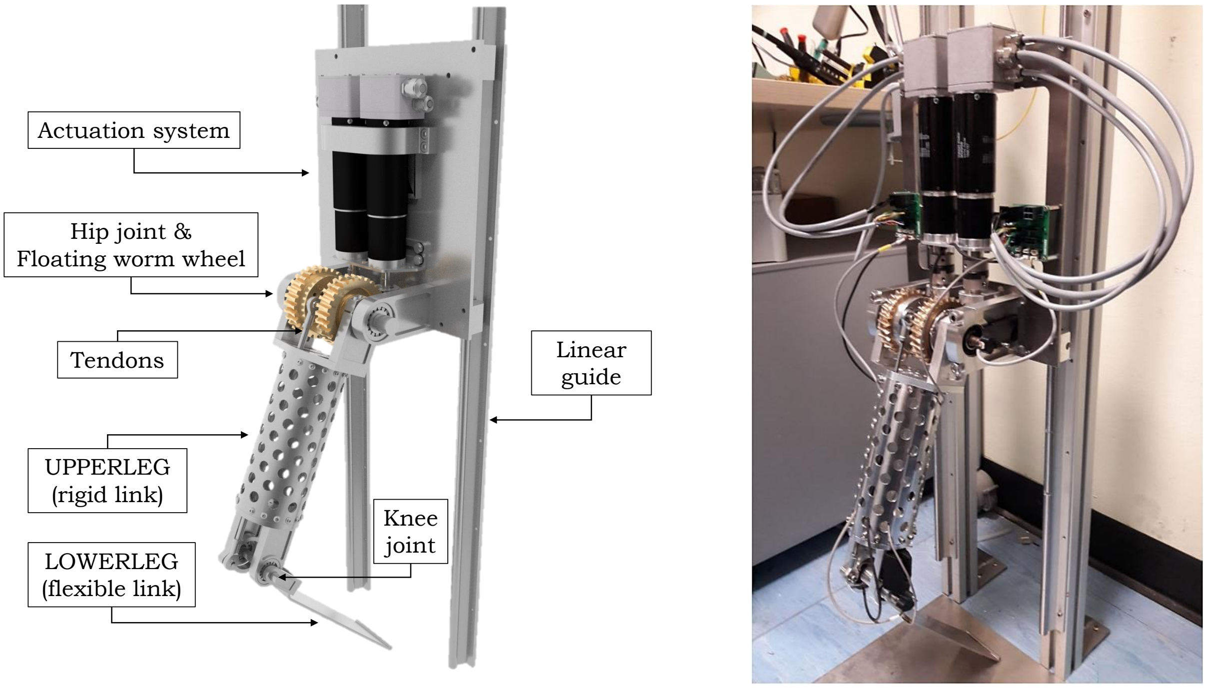

Figure 2.1: FlegX description

The prototype has also been introduced in [11, 14].

2.1 FlegX

FlegX is a 3 DoF underactuated mechanism in witch the two revolute joints, namely hip and knee in Figure 2.1, are actuated, while the third one, the translational joint corresponding to the vertical slider, is not actuated.

2.1.1 Mechanical structure

The upperleg features a biologically inspired mechanical configuration and was conceived as rigid. To minimize the masses, the rigid link was designed as light as possible. It consists of a commercial round thin-wall aluminium tube that features several holes with the purpose of lightening the structure. The tube has an outer diameter of 75mm, an inner diameter of 71mm and a length of 180mm.

The lowerleg, instead, is a flexible link made by stainless steal AISI 304 - X5CrNi18-10 - EN1.4301 of dimensions 250mm x 70mm x 3mm.

Figure 2.2: Flexible link

2.1.2 Actuation system

From the simulations made during the design phase, it came out that, in order to obtain a jump of 5cm, it is necessary to provide to each joint of the leg a torque greater than 70Nm and a speed greater than 40rpm. Taking into account these constraints, it was selected the brushless DC motor EC45 produced by *"Maxon motor Spa"* with a two-stage planetary gearhead GP-42-C with a reduction ratio of 26 : 1. Since the reduction was not sufficient to obtain the desired torque, a further reduction stage of 9.67 : 1 was introduced through a worm gear system.

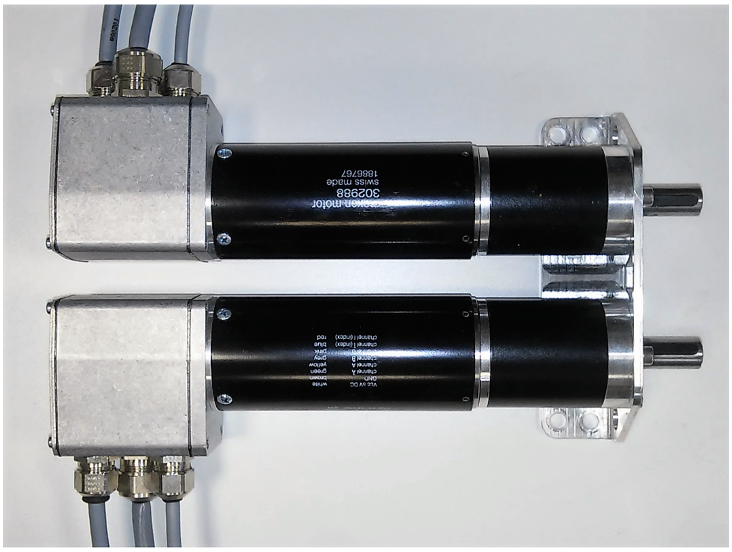

Figure 2.3: Maxon brushless DC motor EC-45 and planetary gearhead GP-42-C

Tables 2.1 and 2.2 summarize the main characteristics stated on the datasheets of the motor and the gearhead.

Table 2.1: EC-45 motor data

Motor data	
Nominal Voltage	$48V$
No load speed	$10700rpm$
No load current	$656mA$
Nominal speed	$10000rmp$
Nominal torque (max. continuous torque)	$316mNm$
Nominal current (max. continuous current)	$7.94A$
Stall torque	$6110mNm$
Stall current	$143A$
Maximum efficiency	87%
Terminal resistance phase to phase	0.336Ω
Terminal inductance phase to phase	$0.149mH$
Torque constant	$42.7mNm/A$
Speed constant	$224rpm/V$
Speed/torque gradient	$1.76rpm/mNm$
Mechanical time constant	$3.85ms$
Rotor inertia	$209gcm^2$

Table 2.2: GP-42-C gearhead data

Gearhead data	
Reduction	$26:1$
Number of stages	2
Maximum continuous torque	$7.5Nm\%$
Maximum intermittent torque	$11.3Nm$
Maximum continuous input speed	$8000rpm$
Maximum intermittent input speed	$8000rpm$
Maximum efficiency	81%
Mass inertia	$9.1gcm^2$

The worm gear system prevents the actuators failure produced by the impulsive torques generated when the leg lands on the ground because the direction of the power transmission is not reversible. The torque applied on the output shaft is balanced by the friction between the worm screw and the coupled gear. The major drawback of this system is its low efficiency.
The worm gears used are the A53U10 produced by *"A.T.T.I. srl"*, Table 2.3 summarize their characteristics.

Figure 2.4: A53U10 worm gears

Table 2.3: A53U10 worm gear data

Worm gear data	
Reduction	9.67 : 1
Lead angle	$13°51'$
Module	2.5
Number of threads	3
Pitch diameter (worm)	$31.29mm$
Tip diameter (worm)	$36.29mm$
Number of teeth	29
Pitch diameter (gear)	$74.71mm$
Maximum diameter (gear)	$82mm$
Inertia (worm)	$3.00\ 10^{-5} kg\ m^2$
Inertia (gear)	$4.81\ 10^{-4} kg\ m^2$

To reduce the leg inertia, the actuation system was located on the linear guide supporting plate.

The motion of the hip and knee joints is decoupled thanks to a floating worm wheel: the hole of the wheel is coupled with a deep groove double row ball bearing that, in turn, has the inner ring constrained to the hip joint shaft.
In order to transmit the motion at the lowerleg, a tendon-like system links the floating worm wheel to the knee joint as shown in Figure 2.5.
As tendons two 280mm-long M4 screws are are used. The tendons are linked to the worm gear and to the knee joint flange by means of spherical bearings.

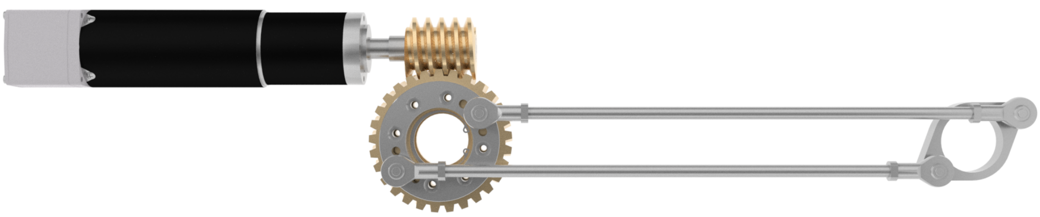

Figure 2.5: Tendon-like system

2.1.3 Sensors

Encoders

The angle of each revolute joint is measured by two magnetic absolute encoders. One is located on the shaft that links the worm gear system to the rigid link, and the other on the shaft that connects the tendon system to the flexible link.
The encoders are the AS5047D produced by *"Austrian Micro Systems"*. They have 14 bit precision and SPI interface. Figure 2.6 shows one of the encoders on top of its support shield and its magnet.

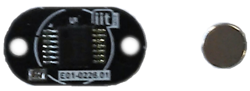

Figure 2.6: Absolute encoder AS5047D

Strain gauge

In order to measure the deflection and the force applied to the flexible link, two strain gauges in half Wheatstone bridge are used. Such a configuration compensates for the effects induced by any axial stress on the element. The sensors are placed on the most stressed part of the flexible link: next to the extreme fixed to the lower revolute joint.
The strain gauges used are produced by *"Vishay"*. They have a grid resistance equal to $120.0 \pm 0.3\%\Omega$ and a gage factor equal to $2.080 \pm 0.5\%$. Figure 2.6 shows one of this two sensors glued on the leg.

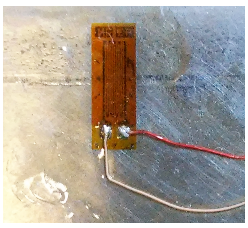

Figure 2.7: Strain gauge

Torque sensors

The leg is equipped with two torque sensors. They measure the torque transmitted from the worm gear system to the upperleg and to the lowerleg. Since the sensors deformation is by far smaller than the flexible link one and to have a linear electrical characteristic, they are composed by four strain gauges in full bridge configuration. Figure 2.8 shows the two sensors used.

Figure 2.8: Torque sensor

2.1.4 Electronic components

Beaglebone Black

The software devoted to the data acquisition and to the execution of the control algorithm is implemented in Simulink®. By means of the model based software design technique, it is loaded on a Beaglebone Black board (shown in Figure 2.9). The board is produced by *"Texas Instrument"* and it runs Debian 7.9 operating system.

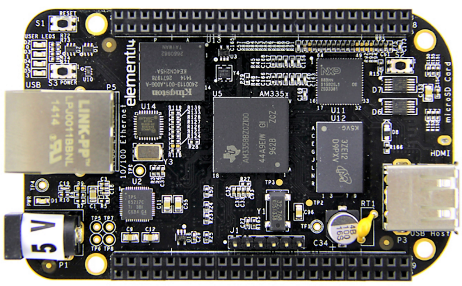

Figure 2.9: Beaglebone Black board

Signal conditioner shield

In order to acquire the sensors' signals, a custom PCB is used. It has the amplifier and filter for the analog sensors and an SPI bus to communicate with the main board.
The shield is shown in Figure 2.10. It has three analog input ports devoted to the encoders and four analog input ports for the strain gauges: ports from number 0 to 2 are devoted to torque sensors (full Wheatstone bridges), while port number 3 is devoted to the flexible link strain gauges (in half bridge configuration). The shield has two trimmers devoted to the bridges tuning for each strain gauge sensor input port.

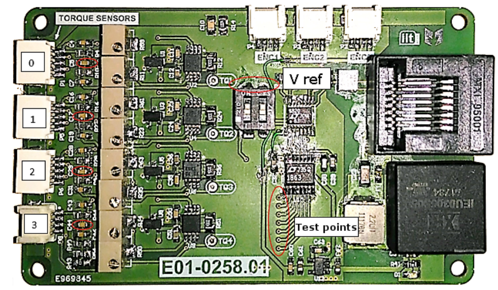

Figure 2.10: Signal conditioner shield

ESCON 70/10 Servo Controller

To drive the motors the *Escon 70/10* servo controller is used. It is a 4-quadrant PWM servo controller that has three different operating modes: speed control (closed loop), speed control (open loop), and current control. It is commanded by an analog input signal and features analog and digital I/O functionality. The device is configured via USB using the graphical user interface *"ESCON Studio"*.

Figure 2.11: Escon 70/10 Servo Controller

2.2 Structure

The leg is constrained to move only along the vertical direction thanks to an aluminium profile structure fixed to the ground. The actuators supporting plate is coupled to this structure by means of two linear guides.

Figure 2.12: Structure

Chapter 3

System characterization

The main goal of the characterization process is to create a model of the leg that can be used during the control design phase.

The analysis of the FlegX starts from the lowerleg subsystem. First, the tendons are re-dimensioned since they were subject to a buckling effect. Then, the flexible link is studied both in statics and in dynamics. The last component of the lower subsystem analyzed is the knee torque sensor. Then, the focus moves on the upperleg and the hip torque sensor is analyzed. Next the leg mechanical properties are either measured or estimated. Finally, the encoders are acquired and calibrated.

3.1 Lower-leg

The lowerleg subsystem is composed by the flexible link, two coupled strain gauges aimed to measure the link deformation, and a torque sensor to measure the torque transmitted from the worm gear system to the knee joint. The motion from the gear to the lowerleg is transmitted by means of a tendon-like system as shown in section 2.1.2.

3.1.1 Tendons dimensioning

Since applying to the knee joint a torque lower than the maximum one found through the jump simulations the tendons were subject to a buckling effect, it has been necessary to re-dimension them.
The tendons are subject only to axial forces because they are linked to the leg through spherical bearings. Starting from the scheme shown in Figure 3.1, it is possible to compute those forces through a torque equilibrium at the center of the joint.

$$T - F_1 \frac{1}{2} b \cos\theta - F_2 \frac{1}{2} b \cos\theta = 0 \tag{3.1}$$

Assuming $|F_1| = |F_2| = F$, the joint angle variation between $-60°$ and $60°$ and the maximum torque applied to the joint around $70Nm$ (derived from the jump simulations), the maximum force the tendons should withstand is computed as follows.

$$F = \frac{T}{b\cos\theta} \quad \rightarrow \quad F_{max} = \frac{T_{max}}{b\cos\theta_{max}} = 2.5kN \tag{3.2}$$

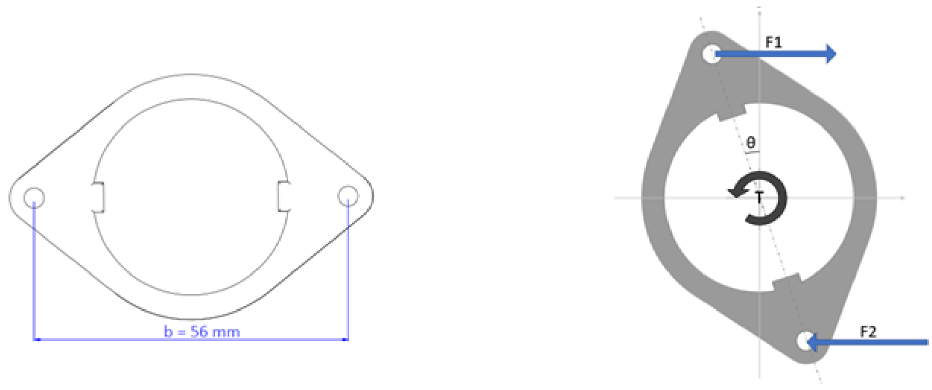

Figure 3.1: Knee joint scheme

The maximum force that can be applied to a bar in order to avoid the buckling effect is computed through the Euler column formula.

$$F_{crit} = \frac{n\pi^2 EI}{L^2} \tag{3.3}$$

With:

$n = 1$ for column pivoted in both ends

E: column elasticity module: $200GPa$

I: moment of inertia of the smallest cross section

L: column length: $L = 300mm$ (including the terminals)

Since the tendons have circular cross section, their inertia is written as

$$I = \frac{\pi}{4} r^4 \tag{3.4}$$

By combining the result obtained in 3.2, equation 3.3 and the relation 3.4 with a proper factor of safety ($C_{FS} = 1.8$), the minimum radius (or diameter) the tendons should have in order to avoid the buckling effect is computed.

$$\frac{\pi^3 E r_{min}^4}{4L^2} = C_{FS} F_{max} \quad \rightarrow \quad r_{min} = \sqrt[4]{\frac{4C_{FS}F_{max}L^2}{\pi^3 E}} \simeq 4.0mm \tag{3.5}$$

The tendons are then substituted with two $8mm$ diameter steal bars.

3.1.2 Strain gauge

In order to measure the flexible link deformation, two strain gauges in an half Wheatstone bridge configuration are used. This layout compensates for the effects induced by any axial stress on the sensors.
The strain gauges are placed on the most stressed part of the flexible link: the area next to the extreme screwed to the rest of the leg.

A-priori information

First, it is necessary to analyze the relations that link the sensors deformation, the tip displacement and the applied force. This is needed to have some a-priori information about their relations and to properly design the identification experiments.
The system is modelled as a cantilever beam as shown in Figure 3.2.

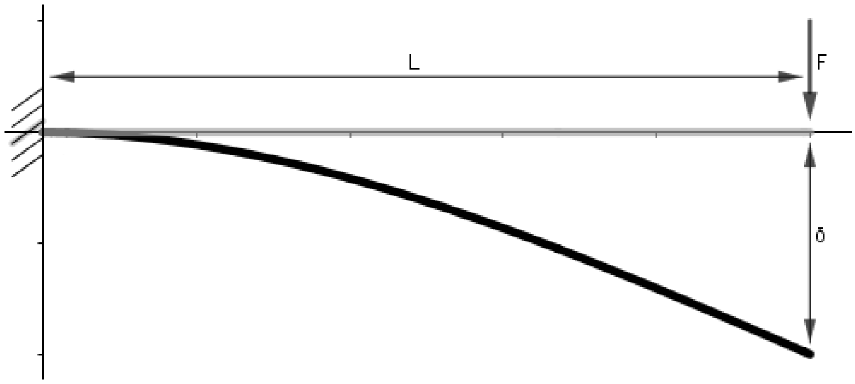

Figure 3.2: Cantilever beam scheme

In statics the displacement of a point placed at a distance x from the fixed joint is computed as

$$\delta(x) = \frac{Fx^2}{6EI}(3L - x) \tag{3.6}$$

With:

- F: magnitude of the orthogonal force applied on the tip of the beam
- L: beam length
- E: beam elasticity module
- I: cross section moment of inertia

The maximum displacement is performed by the tip of the beam and it is equal to

$$\delta_{max} = \frac{FL^3}{3EI} \tag{3.7}$$

Since the link section is rectangular, the moment of inertia is computed as

$$I = \frac{bh^3}{12} \tag{3.8}$$

with b and h the base and height of the beam's section.

Taking into account 3.8 it is possible to rewrite 3.7 as

$$\delta_{max} = \frac{4FL^3}{bh^3E} \tag{3.9}$$

Since only the tip force F is applied, the shear force is constant along the beam. The link is subject to the maximum bending moment at the fixed joint, this is equal to

$$M_{fmax} = FL \tag{3.10}$$

Taking into account 3.8, being the two strain gauges placed next to the fixed joint, the area on with they are placed is subjected to a stress equal to

$$\sigma_{max} = \frac{M_{fmax}}{I}\frac{h}{2} = \frac{6FL}{bh^2} \tag{3.11}$$

The surface deformation measured by the sensors is computed starting from 3.11 as

$$\varepsilon_{max} = \frac{\sigma_{max}}{E} = \frac{6FL}{bh^2E} \tag{3.12}$$

By combining equations 3.11 and 3.12, it is possible to find a relation between the surface deformation read by the strain gauge and the maximum beam deformation.

$$\delta_{max} = \frac{2}{3}\frac{L^2}{h}\varepsilon_{max} \tag{3.13}$$

Equation 3.13 shows that there is a linear relation between the two deformations.

The strain gauges are made by a metallic grid that varies the electrical resistance if stretched or compressed. The relation between the resistance variation ΔR and the deformation ε is described as

$$\frac{\Delta R}{R} = K_s\varepsilon \tag{3.14}$$

With K_s the sensibility constant of the selected strain gauge and R the proper resistance without deformation induced.
The resistance variation produced by the surface deformation is extremely small. In order to convert it in a voltage variation a Wheatstone bridge circuit is used.
The half Wheatstone bridge configuration consists in two strain gauges. One is applied on the top face and the other on the bottom face of the beam. The two deformations are equal but opposite. If the sensors are connected as in Figure 3.3, the signal is doubled with respect to the case of quarter bridge (single strain gauge).

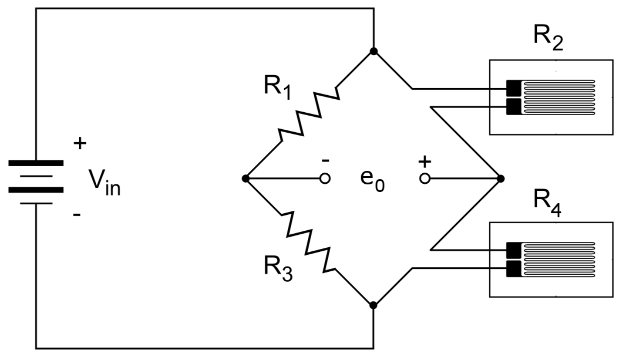

Figure 3.3: Half Wheatstone bridge scheme

Referring to Figure 3.3, the bridge consists in two strain gauges (R_2 and R_4) and two fixed resistors (R_1 and R_3), it is powered by a voltage V_{in} and the output voltage is e_0.

$$e_0 = \frac{R_1R_4 - R_2R_3}{(R_1+R_3)(R_2+R_4)}E \tag{3.15}$$

Taking into account the strain gauge characteristic stated in relation 3.14, the equation 3.15 can be rewritten as

$$e_0 = \frac{R_1(R_4 + \Delta R) - (R_2 - \Delta R)R_3}{(R_1 + R_3)((R_2 - \Delta R) + (R_4 + \Delta R))}E \tag{3.16}$$

If the bridge is compensated $R_1 = R_2 = R_3 = R_4 = R$, recalling the relation 3.14, the output signal becomes

$$e_0 = \frac{R(R + \Delta R) - (R - \Delta R)R}{2R((R - \Delta R) + (R + \Delta R))}E = \frac{1}{2}\frac{\Delta R}{R}E = \frac{1}{2}K_s\varepsilon E \tag{3.17}$$

Equation 3.17 shows that there is a linear relation between the surface deformation and the output signal.

Taking into account the relations 3.13 and 3.17, the relation between the tip displacement and the output signal comes out to be linear. Such a characteristic can be found by means of an identification process.
Furthermore, since during the calibration phase the force F is known and since, as demonstrated by equation 3.12, there is a constant relation between the maximum beam deformation and the load applied to its tip, it is also possible to determine the relation between the sensor readings and the force F.

Test bench realization

In order to properly calibrate the strain gauge, it is necessary to apply to the flexible element a fully known force, measure the tip displacement and read the corresponding sensor output.
It has been decided to use Bosch profiles to build the test bench because of the modularity and the easy assembly. This allows to reshape the bench for each experiment quickly and without the need of designing new pieces.
With the structure shown in Figure 3.4, it is possible to fix the flexible element horizontally as in the analysis of the cantilever beam and, on top of it, the laser sensor devoted to the displacement measurements.

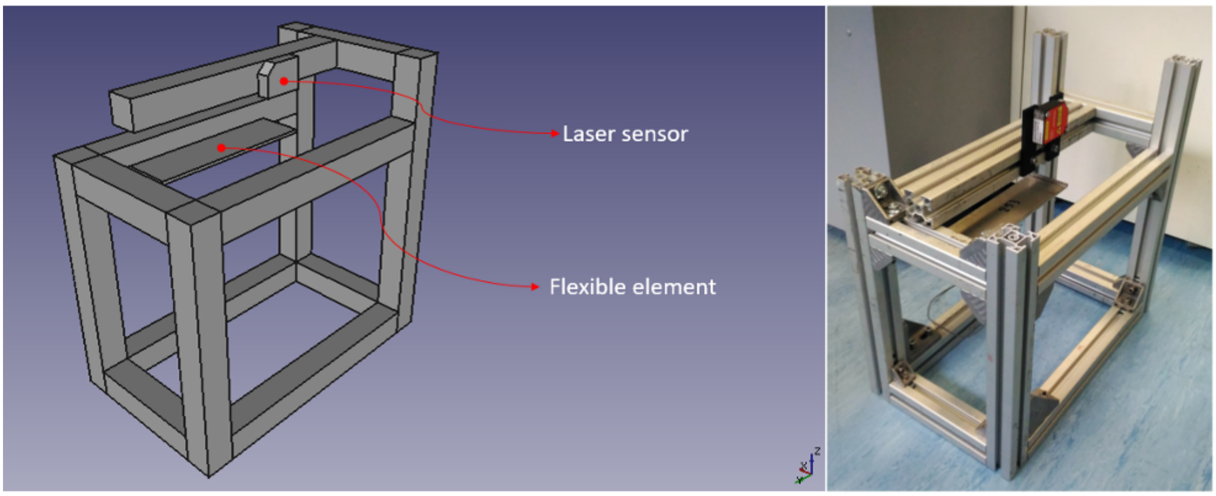

Figure 3.4: Strain gauge calibration test bench

Strain gauge characteristic identification

As shown in Figure 3.5, the force is applied by hanging different weights to the tip of the flexible element, at $243mm$ from the fixed face. The displacement is measured next to the force application point, at $238.5mm$ from the fixed face, through the laser sensor. Its output voltage along with the strain gauge signal is acquired through the oscilloscope.

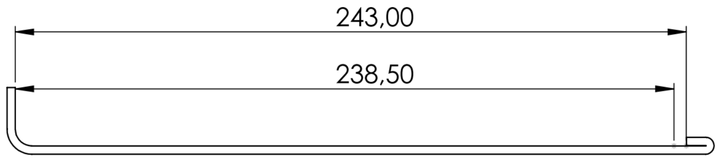

Figure 3.5: Flexible link test set-up representation

Even if the test bench has been built as rigid as possible, subject to such forces, its deformation can not be neglected. To evaluate the constraint deformation order of magnitude, some weights are hanged to the tip of the beam and the displacement of different points of the fixed face are measured through the laser sensor as shown in Figure 3.6.

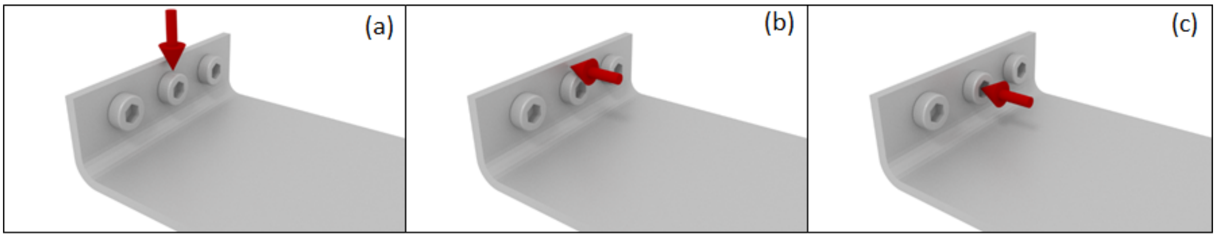

Figure 3.6: Constraint deformation measures: (a) vertical displacement, (b) and (c) horizontal displacement

Referring to Figure 3.6, applying to the tip of the link $95.16N$ the displacement is about $0.11mm$ for case (a), $-8.75\ 10^{-2}mm$ for case (b) and $-2.5\ 10^{-2}mm$ (equal to the laser sensitivity) for case (c). Taking into account the geometrical dimensions and the obtained measures, graphically, the constraint deformation has been estimated to be around $1.10\ 10^{-4}rad/N$.

Considering the constraint deformation, it is possible to compare the measure of the link displacement with the FEM analysis performed during the mechanical design phase. The simulation data is provided by dott. Cristiano Pizzamiglio.
The linear characteristic describing the relation between the tip displacement and the applied force is derived using the least squares identification method both for the experimental and numerical case. The results are shown in Figure 3.7.

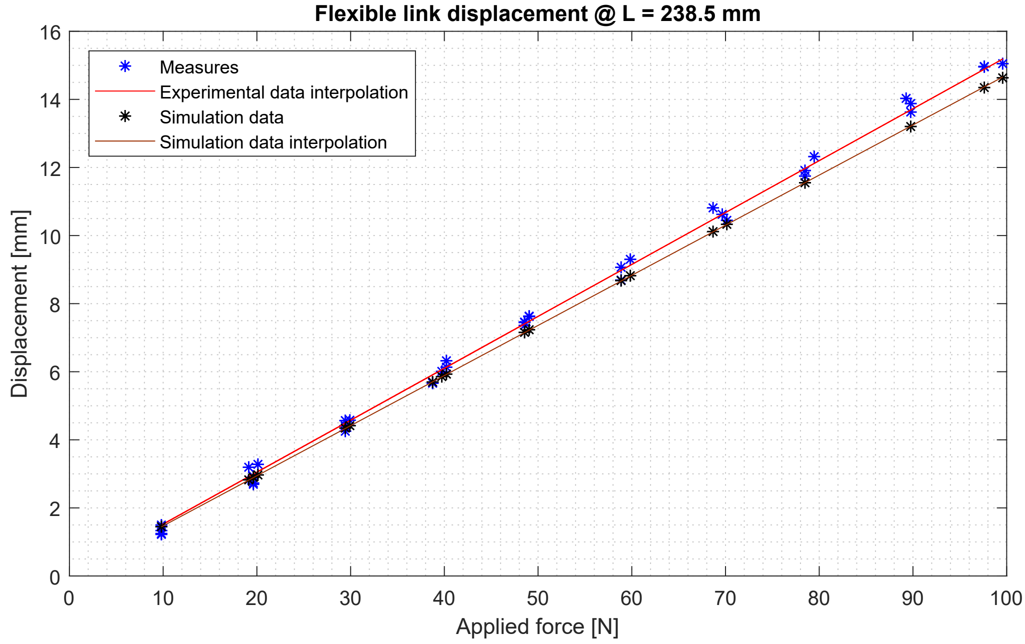

Figure 3.7: Flexible link tip displacement data comparison

The difference between the two characteristics is of 3.48% with respect to the experimental one.

The Force-Voltage relation is analyzed by following three different approaches.
The first approach considers the output error model, which consists in summing the error as a random variable with zero mean value directly to the system output, as shown in Figure 3.8. The system output y is computed as $y = \Phi\theta_0 + e$, with Φ the input data matrix and θ_0 the G system parameters array.

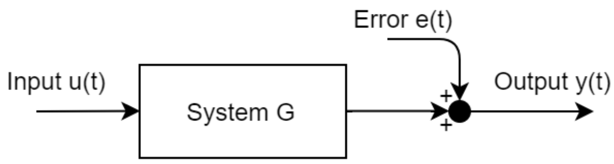

Figure 3.8: Output error system model

The parameter estimate is derived through the least squares approach, the simplest one from the computational point of view.

$$\hat{\theta}_{LS} = \left[\Phi^T \Phi\right]^{-1} \Phi^T y \tag{3.18}$$

By applying the least squares algorithm to the collected data, the system model results to be $y(t) = 17.86\ u(t) - 0.05$. Such a characteristic is compared with the collected data in Figure 3.9.

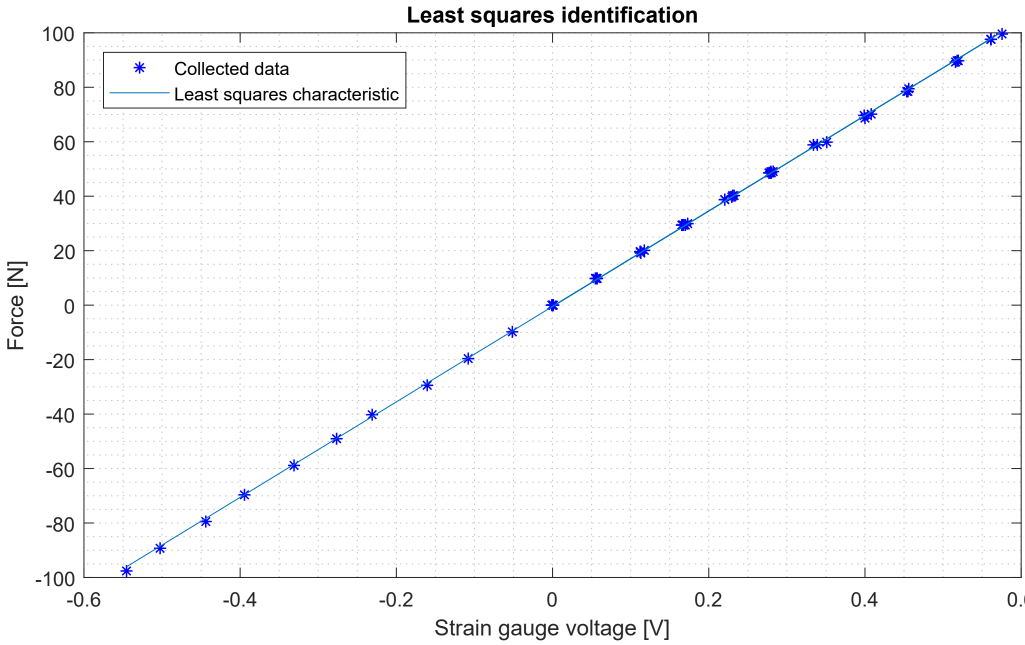

Figure 3.9: Least squares characteristic

The second method considers the output error model in the set membership identification framework. Since the noise derives from physical sensors, the error is assumed to be componentwise bounded: $|e(t)| \leq e_0$. The system model is the same depicted in Figure 3.8 and the mathematical model is $y = \Phi\theta_0 + e$, with Φ the input data matrix and θ_0 the G system parameters array. The parameter uncertainty interval (PUI) of such a problem is computed through the linear programming solver available in MATLAB. The linear characteristic is found as the Chebyshev center of the PUI. The resulting system model is $y(t) = 17.92\ u(t) - 0.07$. The characteristic is compared with the collected data in Figure 3.10.

The third and last approach is the most complete one because it considers the error in variable model. This model takes into account not only the output error introduced by the acquisition system but also the one due to the uncertainty on the applied input. The model of the considered system is shown in Figure 3.11.

Both the input and the output errors are assumed to be componentwise bounded: $|\epsilon(t)| \leq \epsilon_0$ and $|\mu(t)| \leq \mu_0$. Since them enter the problem in a non-linear way the method turns into a polynomial optimization problem. Its parameter uncertainty interval (PUI) is computed through the SparsePOP software. The characteristic parameters is derived as the Chebyshev center of the PUI and it turns out to be $y(t) = 17.92\ u(t) - 0.07$. The characteristic is compared with the collected data in Figure 3.12.

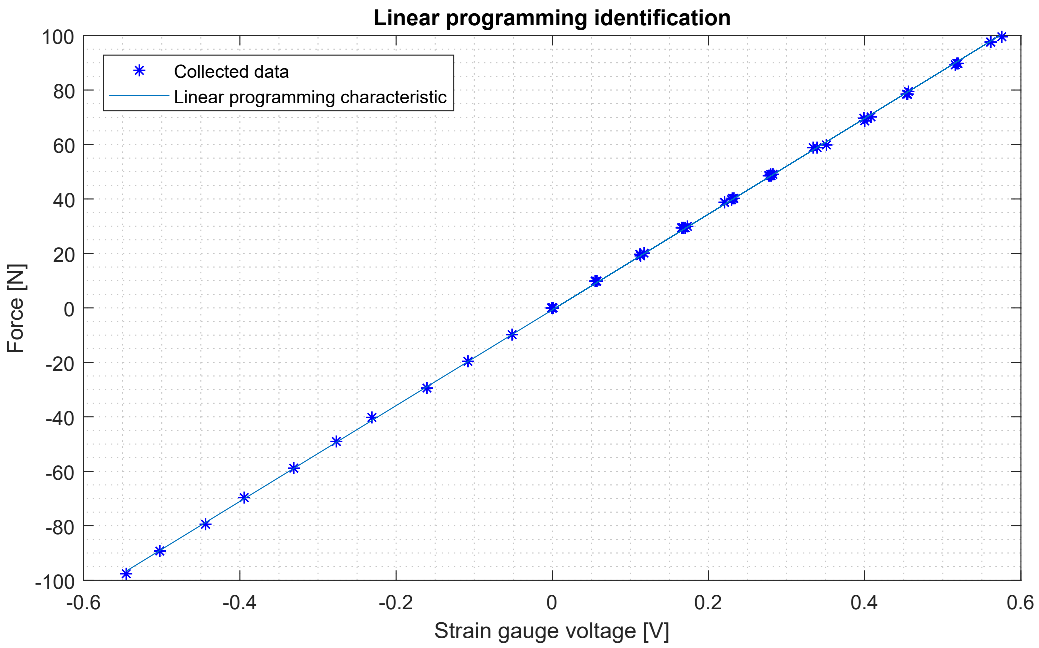

Figure 3.10: Linear programming characteristic

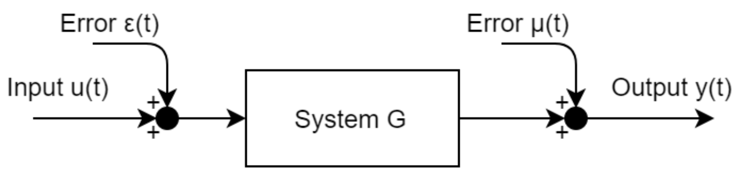

Figure 3.11: Error in variable system model

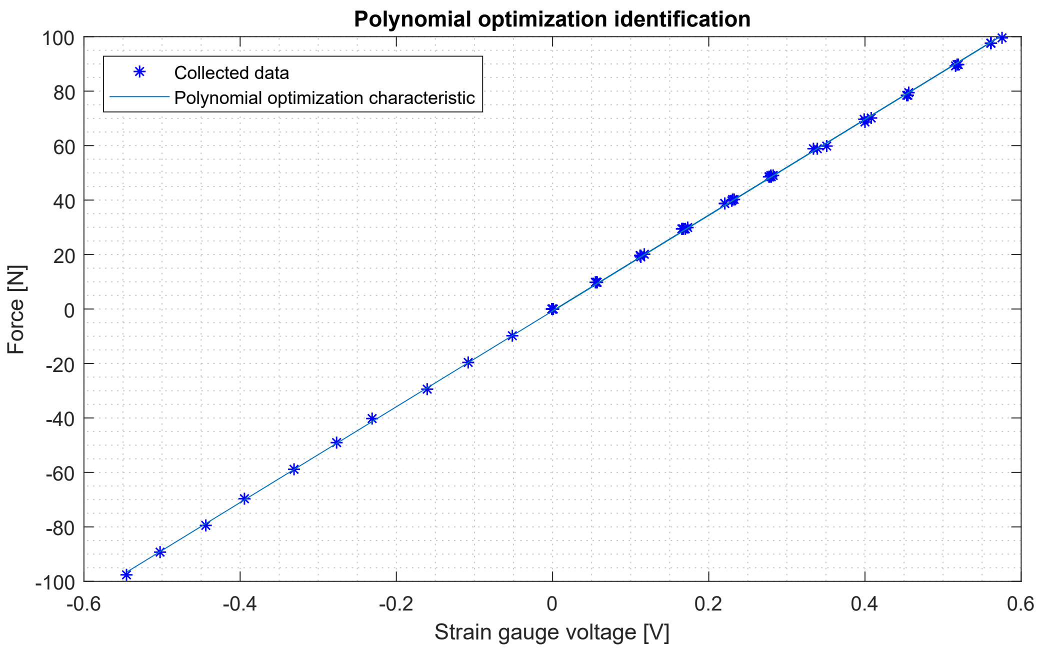

Figure 3.12: Polynomial optimization characteristic

The three characteristics are compared in Figure 3.13. The difference of the first two methods is computed with respect to the the polynomial optimization model: 0.33% for the least squares one and 0.01% for the linear programming one.

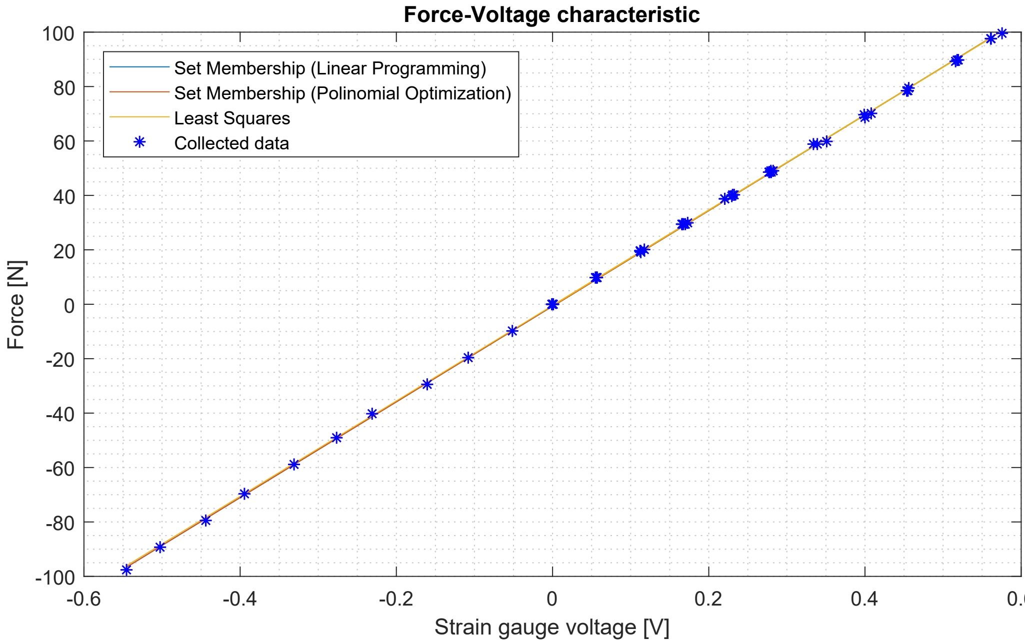

Figure 3.13: Force-Voltage characteristic

Seen the minimal differences between the results and the extreme simplicity from the computational point of view of the first approach with respect to the other two, for the linear characteristic identifications the least squares method is used.

3.1.3 Flexible link dynamics

To evaluate the flexible link dynamical properties, different vibrational responses to impulsive forces are collected and examined. Where possible the results are compared to the theoretical ones computed through the FEM analysis performed during the mechanical development phase. The FEM data shown in this chapter is provided by dott. Cristiano Pizzamiglio.
While the amplitude of the tip displacement due to the oscillations decreases quickly as the frequency increases, the detection of the natural frequencies higher than the first couple are difficult. To check the strain gauge measurements an accelerometer is used since the acceleration measurement has an higher frequency range content.
The test bench configuration shown in Figure 3.4 has been modified, the laser sensor is removed and an accelerometer is placed on the tip of the beam.
To be sure to urge all the first natural modes of vibrating the link is divided in five sections and it is hit at each division with an impact hammer. An example of the collected data is shown in Figure 3.14.

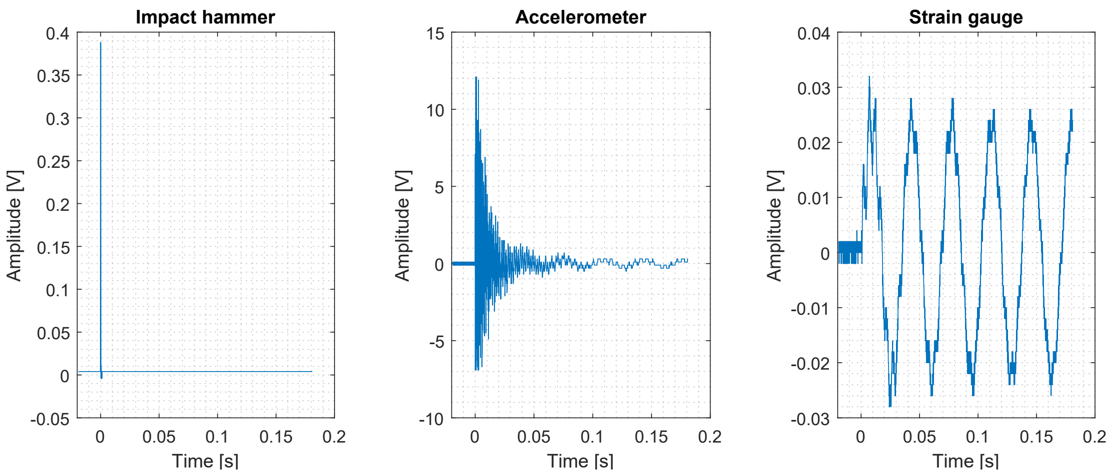

Figure 3.14: Flexible link impulse response (Set 1)

Through the Fourier analysis of the acquired signals, the impulse frequency response of the flexible link is derived for both the tip acceleration measured by the accelerometer and the displacement acquired through the strain gauge. The resulting plot is shown in Figure 3.15.

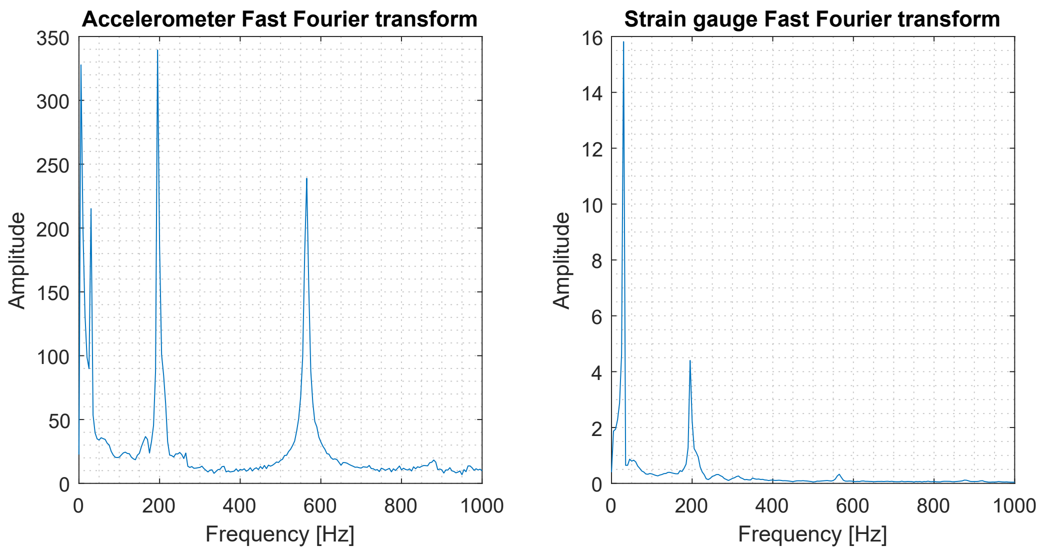

Figure 3.15: Accelerometer and strain gauge frequency response (Set 1)

From the frequency analysis, the first three natural frequencies associated to non-planar modes of vibrating are derived.

Table 3.1: First three flexible link natural frequencies (Set 1)

Vibration mode	**Accelerometer measure**	**Strain gauge measure**
I	30 Hz	30 Hz
II	195 Hz	195 Hz
III	565 Hz	565 Hz

The accelerometer senses also a low-frequency signal, this can be caused by the non-ideal test bench used during the measurements.

Since the accelerometer has a not-null mass, the frequencies are affected by the added weight. To evaluate the real ones the sensor is removed and the analysis is repeated with only the measures of the strain gauge.
The flexible link is divided in eight sections in order to have more detailed information about the modal shapes. An example of the collected data is shown in Figure 3.16.

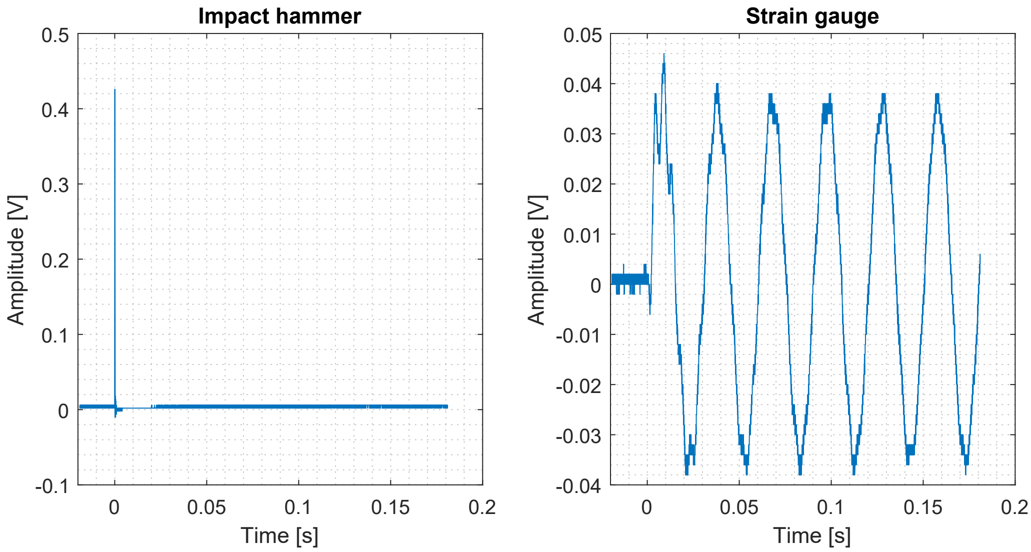

Figure 3.16: Flexible link impulse response (Set 2)

Again through the Fourier analysis of the acquired signals, the impulse frequency response of the flexible link is derived only for the displacement acquired through the strain gauge, the resulting plot is shown in Figure 3.17.

From the frequency analysis, the firs three natural frequencies associated to non-planar modes of vibrating are derived.

Table 3.2: First three flexible link natural frequencies (Set 2)

Vibration mode	**Strain gauge measure**
I	35 Hz
II	210 Hz
III	585 Hz

The derived frequencies are compared to the theoretical ones computed through FEM analysis performed during the mechanical design phase in Table 3.3.

Table 3.3: First three flexible link natural frequencies comparison

Vibration mode	**Measure Set 1**	**Measure Set 2**	**FEM analysis**
I	30 Hz	35 Hz	39 Hz
II	195 Hz	210 Hz	241 Hz
III	565 Hz	585 Hz	676 Hz

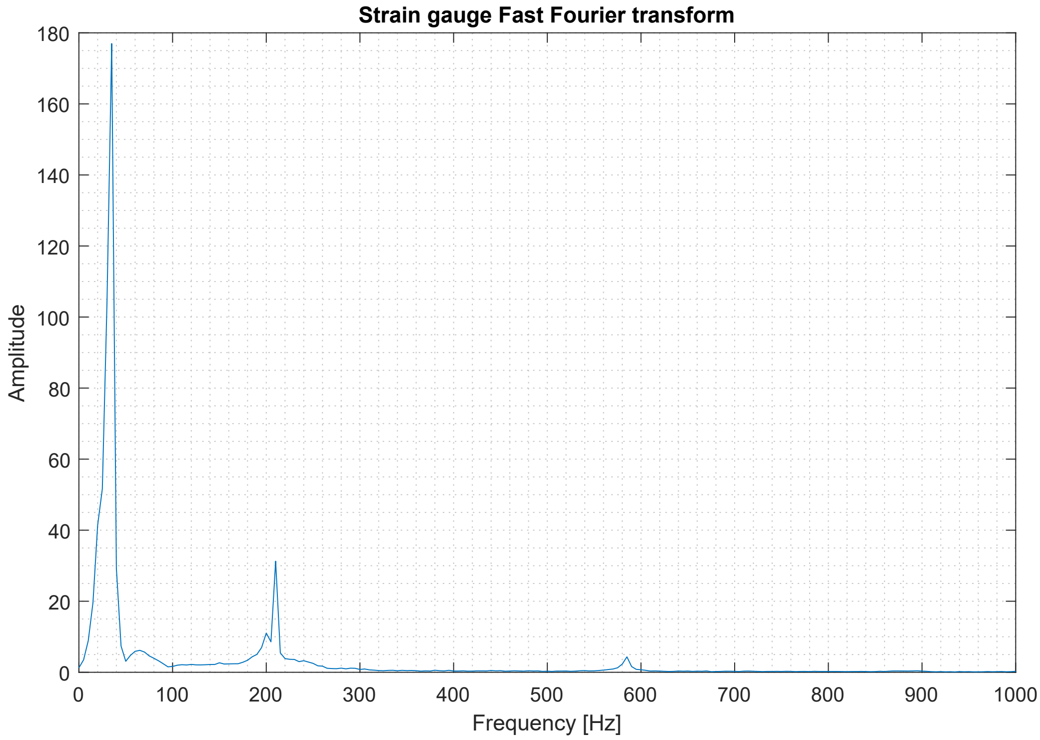

Figure 3.17: Strain gauge frequency response (Set 2)

The difference between the frequencies obtained through the two sets derives from the presence of the accelerometer on the tip of the link during the first measurement campaign. Taking into account the approximate formulas for natural frequencies of systems having both concentrated and distributed mass stated in [15], the effect of the accelerometer mass is analyzed.
The natural frequency of a uniform cantilever beam with a mass on the end is computed as:

$$\begin{aligned} f_n &= \frac{1}{2\pi}\sqrt{\frac{k}{M+0.23m}} \\ k &= \frac{3EI}{L^3} \end{aligned} \tag{3.19}$$

With:

M : the concentrated mass on the tip of the beam

m : the link mass

E : the Young modulus

I : the beam inertia $I = \dfrac{bh^3}{12}$

L : the link length

b : the link width

h : the link thickness

The formula stated in (3.19) can be used also to compute the expected first natural frequency without a concentrated mass:

$$f_{1,\ expected} = \frac{1}{2\pi}\sqrt{\frac{k}{0.23m}} = 37.26\ Hz \tag{3.20}$$

The obtained value is in between the experimental one (second set) and the FEM one. In order to evaluate the effect of the added concentrated mass, first, the experimental equivalent mass ($m_{eq} = 0.23m$) is computed from the frequency measure as $m_{eq} = \frac{k}{(2\pi f_1)^2} = 0.13kg$. Then, the formula (3.19) is applied taking into account the accelerometer mass and the corrected first natural frequency is computed:

$$f_{1,\ corrected} = 30.19\ Hz \tag{3.21}$$

The result shown in (3.21) is very close to the experimental one ($f_1 = 30Hz$), this shows that the obtained difference is due to the presence of the accelerometer on the tip of the beam during the first set of measurements.

Analysing the frequency response of the beam excited at each division, the modal shapes for the three natural frequencies are reconstructed. The obtained results are compared with the theoretical ones obtained from the FEM analysis performed during the mechanical design phase.

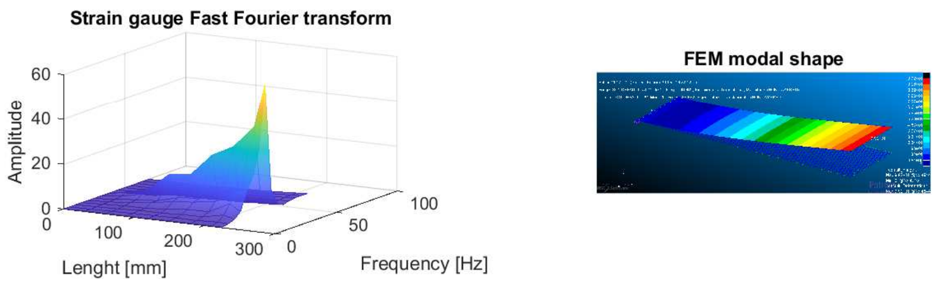

Figure 3.18: First modal shape: experimental and theoretical results

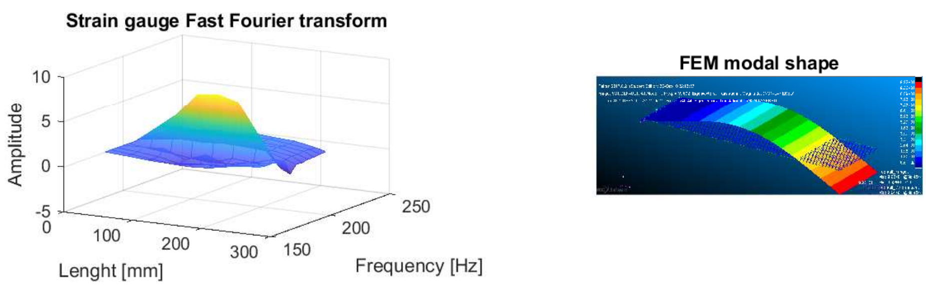

Figure 3.19: Second modal shape: experimental and theoretical results

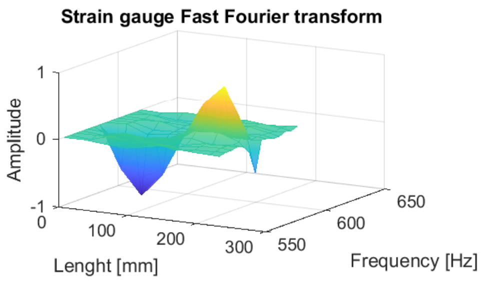

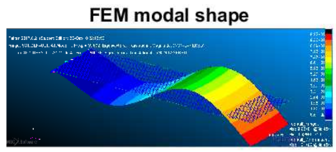

Figure 3.20: Third modal shape: experimental and theoretical results

3.1.4 Knee torque sensor

Experiment set-up

To calibrate the knee torque sensor, it is necessary to apply to it a known torque and measure its corresponding output.
The previously used test bench has been modified, the leg support has been clamped to it and the lowerleg tip has been fixed in order to prevent any movement, as shown in Figure 3.21. The torque is applied by the knee joint motor driven with a current control (torque control). Since between the motor and the considered sensor there is the worm gear system whose characteristic is not known, the transmitted torque is not computable a-priori, then it is measured through the already calibrated strain gauge.

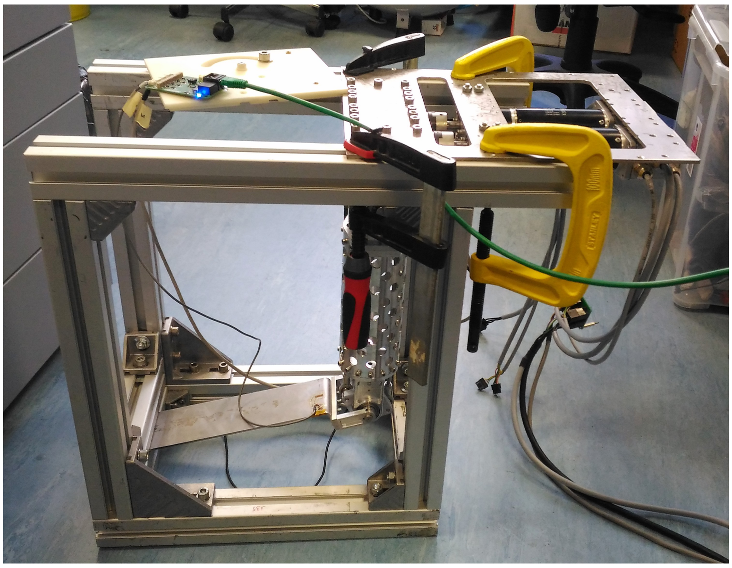

Figure 3.21: Knee torque sensor calibration test bench

Characteristic identification

By setting different current reference values to the knee joint motor, the corresponding force readings provided by the strain gauge and torque sensor voltages are collected. The applied torque is computed starting from the measured force and taking into account the lower link length.
The acquired data is shown in Figure 3.22.

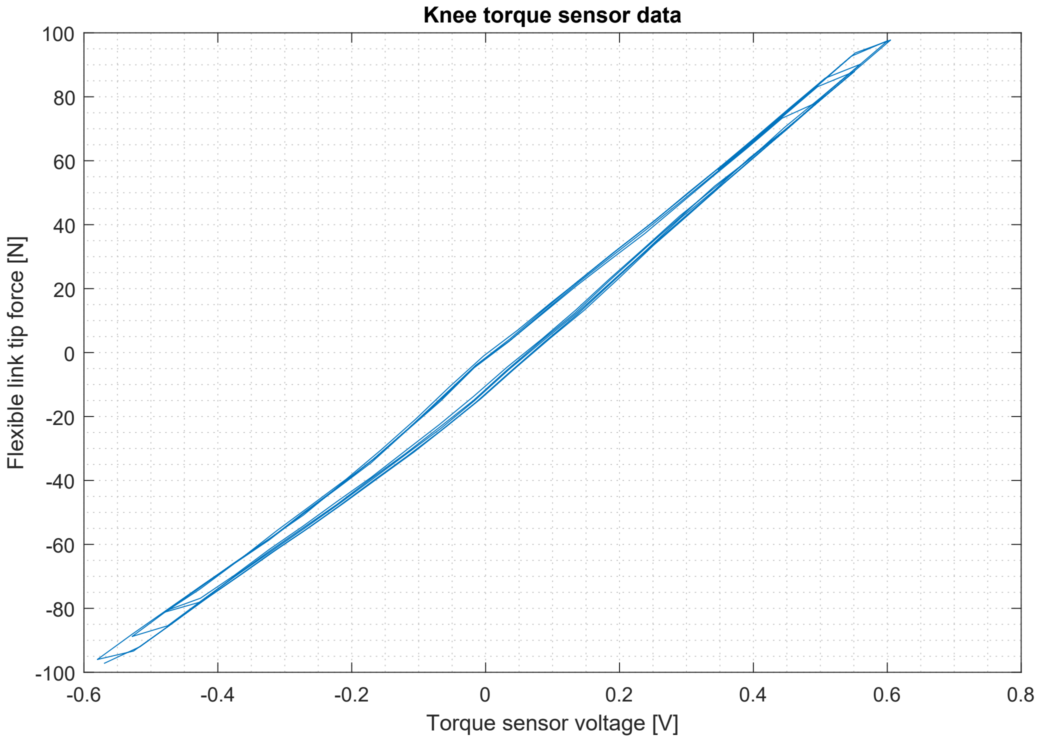

Figure 3.22: Knee torque sensor data

The simplest model that describes the collected data is a single linear characteristic. This is computed through the least squares method upon all the data points. By taking into account the sensor voltage as input (u) and the applied torque as output (y) the characteristic is computed.

$$y = 47.69\ u - 1.56 \tag{3.22}$$

Since from Figure (3.22) it is evident that the sensor is affected by hysteresis, a more complex but more accurate model is computed. Dividing the increasing-torque data from the decreasing-torque one, two separate characteristics are computed for the two cases. Depending on the input derivative sign the output y_i is used for increasing voltages and y_d for decreasing ones.

$$\begin{aligned} y_i &= 48.03\ u - 2.46 \\ y_d &= 47.79\ u - 0.60 \end{aligned} \tag{3.23}$$

The two computed models are compared upon the collected data in Figure 3.23 .Depending on the accuracy of the measures needed by the sensor usage one of them will be chosen at the expense of computational simplicity.

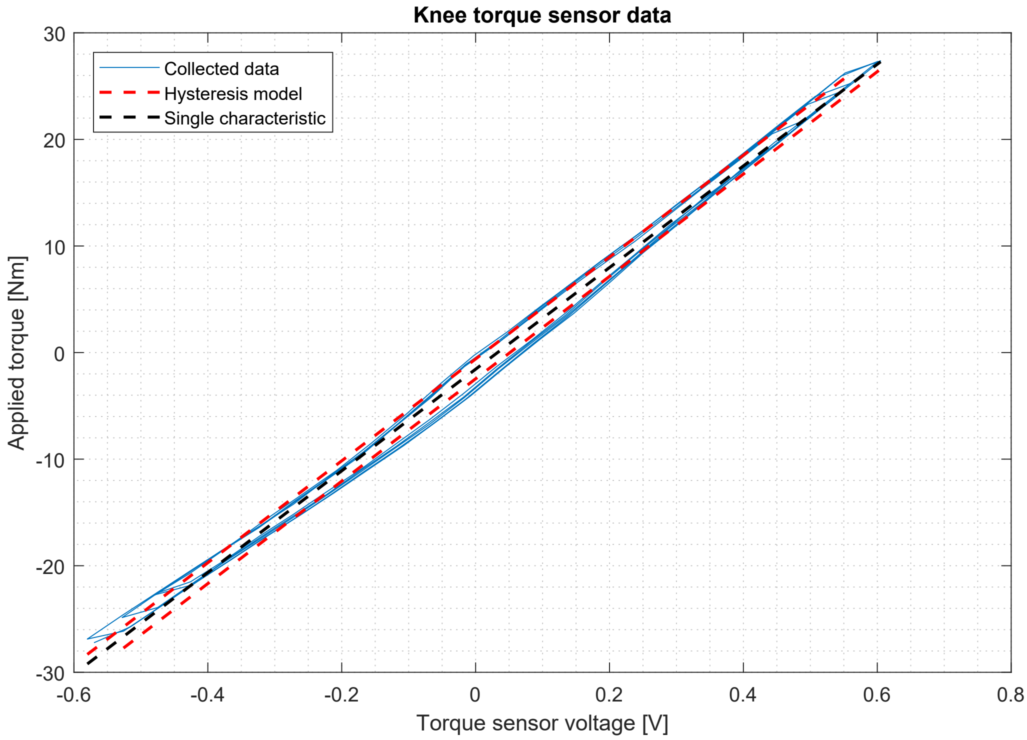

Figure 3.23: Knee torque sensor models

3.2 Upper-leg

The upperleg subsystem is composed by the rigid link and a torque sensor devoted to the measurement of the torque transmitted from the worm gear system to the hip joint.

3.2.1 Hip torque sensor

Experiment set-up

To calibrate the hip torque sensor, it is necessary to apply to it a known torque and measure its corresponding output.
The test bench has been modified, the leg support has been clamped to it and the lowerleg subsystem has been removed. To fix the upperleg rotation and to measure the transmitted torque, a load cell has been connected between the knee joint and the bench as shown in Figure 3.24. In order to acquire at the same time both the torque sensor voltage and the force sensed by the load cell, the last one has been connected to the acquisition shield (BeagleBone Black) through a voltage follower. This has been powered with $V_s^- = 0V$ and $V_s^+ = 3.3V$ in order to avoid extra-voltages that could damage the board.

The torque is applied by the hip joint motor driven with a current control (torque control).

Characteristic identification

By setting different current reference values to the hip joint motor, the corresponding force readings provided by the load cell and torque sensor voltages are collected. The applied torque is computed starting from the measured force and taking into account the

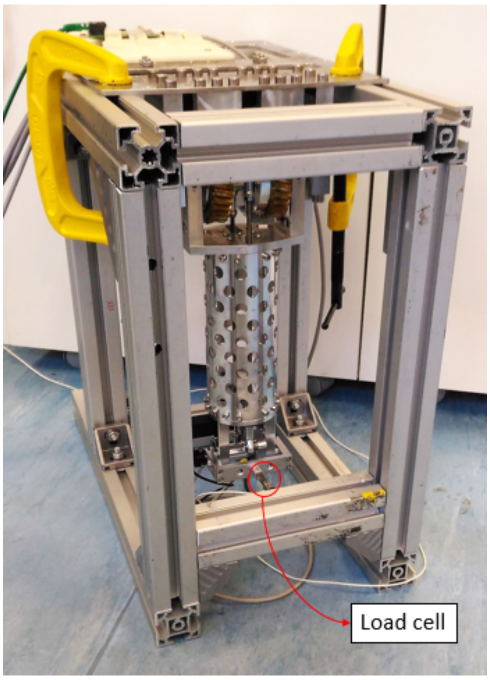

Figure 3.24: Hip torque sensor calibration test bench

upper link length.
A first set of collected data showed that the hip torque sensor is affected by an hysteretic behaviour more pronounced with respect to the knee one. In order to identify a good model for the sensor, it is necessary to acquire a lot of data. For this, an automatic process was created through a Simulink model. This brings to a faster and more precise data acquisition. The motor is actuated through a ramp reference signal between a maximum and a minimum values. Different data sets have different extreme values in order to analyze the hysteretic effect. The collected data is shown in Figure 3.25 where the different data sets are represented in different colors to evidence the sensor behaviour.

By analysing the collected data, a good model that can describe the sensor behaviour is composed by two different linear characteristics, one for the increasing torque data and another one for the decreasing one. The transition between the two is performed in an interval of $V_{tr} = 0.2V$ following a moving characteristic with constant gain. The data is subdivided by extracting the first values inside a range of $0.2V$ after a change of voltage trend and grouping them as transition points. Then, the increasing voltage data is divided from the decreasing one. Each group is processed with the least squares identification method to find the three different characteristic: y_i for increasing voltages, y_d for decreasing ones and y_{tr} for the transition points.

$$\begin{aligned} y_i &= -44.37\ u - 1.74 \\ y_d &= -42.16\ u + 1.96 \\ y_{tr} &= -54\ u + c \end{aligned} \tag{3.24}$$

The transition characteristic offset c is computed by imposing its passage for the last monotone point of a set.

The three characteristics are compared upon the collected data in Figure 3.26, the transition characteristic offset c is set as example to zero.

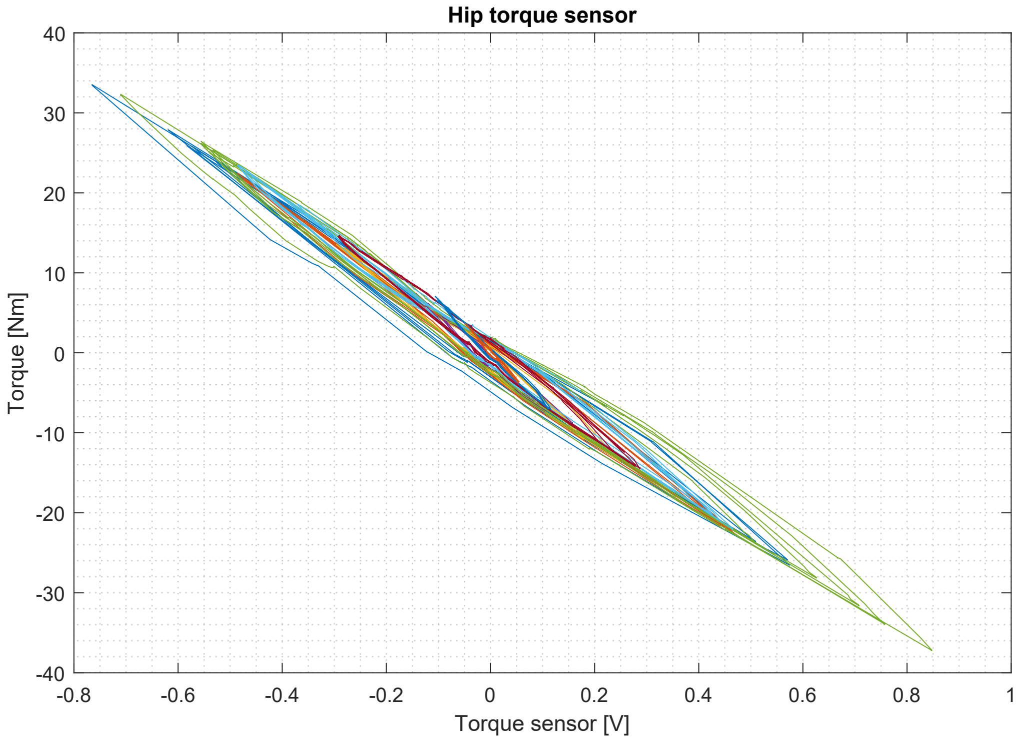

Figure 3.25: Hip torque sensor data

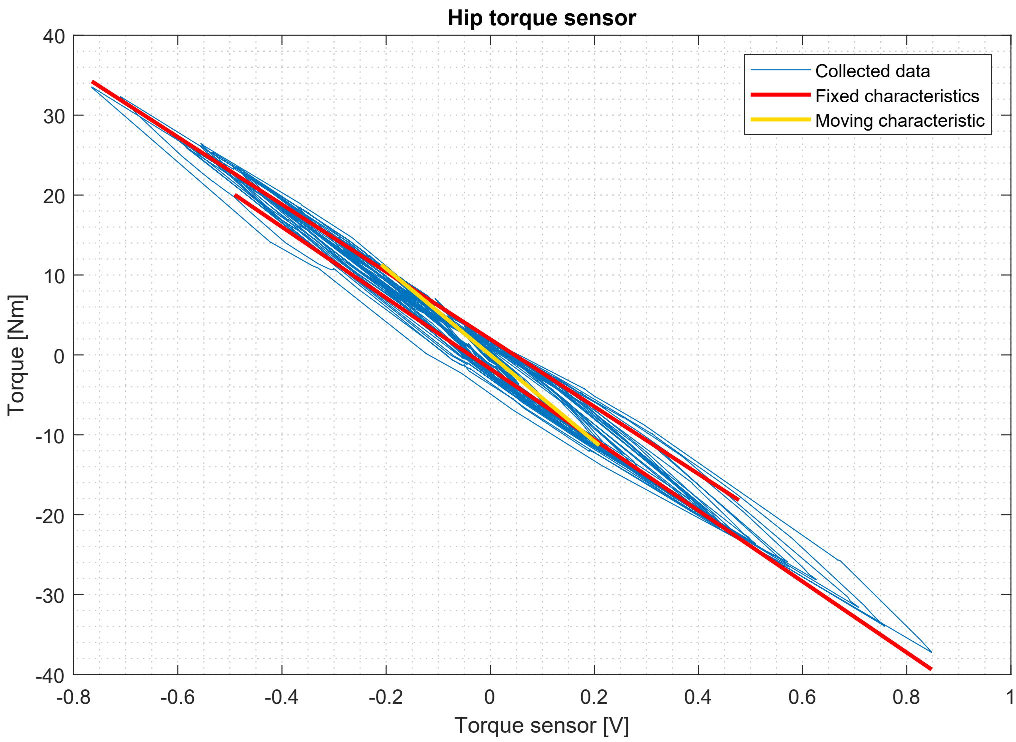

Figure 3.26: Hip torque sensor model

3.3 Mechanical properties

Since the leg can not be totally disassembled, the masses and inertias identification process focused on three main subsystems: the leg support, the upperleg and the lowerleg.
The last two refer to the components that are connected after the respective torque sensors. The first subsystem is composed by the linear guide supporting plate, the hip shaft supports, the two worm gears, the power system and the electronic components. The second one includes the rigid link, the hip and knee shafts, the tendon-like system and the hip and knee torque sensors. The last one is composed by the flexible link, the knee shaft, the small link between the two and the knee torque sensor.

3.3.1 Leg support

Since the leg support is constrained to move only along the vertical axis, the only physical dimension of interest is its mass. This, measured with a weight scale, results to be around $6.6kg$.

3.3.2 Physical pendulum equations

For the two rotating subsystems, the inertia can be measured removing the worm gears and considering them as physical pendulums.
The torque equilibrium referred to the rotation axis of the physical pendulum, as shown in Figure 3.27, taking into account also the joint friction, is:

$$mgL_{cm}\sin\theta(t) + c\dot{\theta}(t) + I\ddot{\theta}(t) = T(t) \tag{3.25}$$

With m the pendulum mass, L_{cm} the distance of the center of mass from the rotation axis, c the joint friction and I the pendulum inertia around the rotation axis.

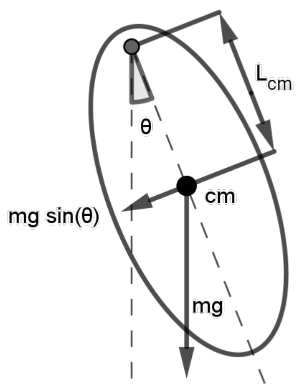

Figure 3.27: Physical pendulum schematic

With the small oscillation theory assumptions, it is possible to approximate linearly the non-linear functions by replacing them with their second order Taylor series around the working point. In equation (3.25) $\sin\theta(t)$ is replaced with $\theta(t)$.
By applying the Laplace transform the torque equilibrium becomes:

$$mgL_{cm}\theta(s) + sc\theta(s) + s^2I\theta(s) = T(s) \tag{3.26}$$

The second order transfer function between the applied torque T and the angle θ is:

$$\frac{T(s)}{\theta(s)} = \frac{k}{s^2 + 2\zeta\omega_n s + \omega_n^2} = \frac{1/I}{s^2 + \frac{c}{I}s + \frac{gmL_{cm}}{I}} \tag{3.27}$$

From equation (3.27), the relations between the inertia I, the friction coefficient c and measurable quantities is derived.

$$I = \frac{mgL_{cm}}{\omega_n^2} \tag{3.28}$$

$$c = 2\zeta\omega_n I \tag{3.29}$$

The natural frequency ω_n and the damping factor ζ are derived from the free oscillations as stated by [16], by measuring the pick amplitude of the i-th period a_i, the oscillations frequency f and computing:

$$\delta = \frac{1}{n}\log\frac{a_i}{a_{i+n}} \tag{3.30}$$

$$\omega_n = \sqrt{4\pi^2 + \delta^2} f \tag{3.31}$$

$$\zeta = \frac{\delta^2}{\sqrt{4\pi^2 + \delta^2}} \tag{3.32}$$

3.3.3 Upperleg

Since the two gears are not removable and their mechanical properties are known from the producer datasheet, the subsystem mass and inertia are measured with them connected. Then, thanks to the superposition of the effects, their contribution can be removed.
The total mass is measured by means of a weight scale and it results to be $m_{tot,upperleg} = 2.97kg$. The upperleg mass is computed removing the gear masses and it is $m_{uppeleg} = 1.93kg$.
The center of mass is derived by measuring the torque applied to the hip torque sensor. The upperleg is placed horizontally and the measured torque is divided by the subsystem weight force. The measured torque is $T_{upperleg} = 2.48Nm$ and the center of mass results to be $L_{cm,upperleg} = \frac{T_{upperleg}}{m_{upperleg}\ g} = 0.13m$.
Through the superposition of the effects the total center of mass is computed as:

$$L_{cm,tot} m_{tot,upperleg} = L_{cm,upperleg}\ m_{upperleg} + 2L_{cm,gears}\ m_{gear} \tag{3.33}$$

Since the distance of the gears center of mass from the hip shaft is null, the relation becomes $L_{cm,tot} = \frac{L_{cm,upperleg}\ m_{upperleg}}{m_{tot,upperleg}} = 8.40 \cdot 10^{-2}m$.

From the free oscillations shown in Figure 3.28, the parameter δ is computed accordingly to equation (3.30) and the frequency f is measured. The resulting values are $\delta = 0.37$ and $f = 1.01Hz$. Therefore, the natural frequency and and the damping factor are derived as stated in equations (3.31-3.32): $w_n = 6.38rad/s$ and $\zeta = 2.18 \cdot 10^{-2}$.

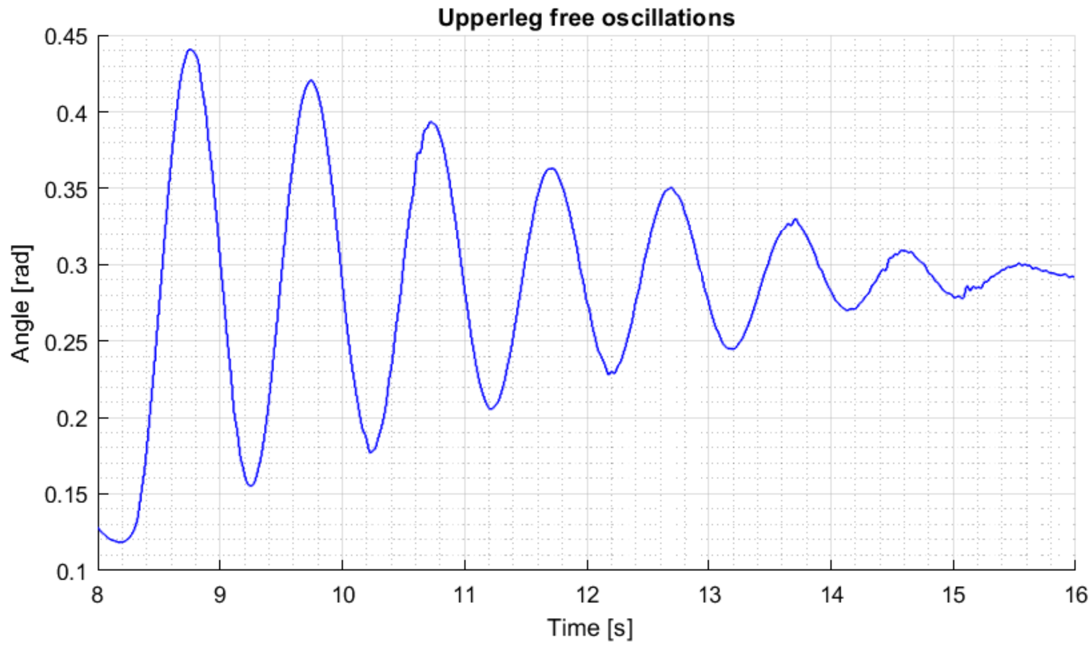

Figure 3.28: Upperleg free oscillations

By means of equation (3.28), the total subsystem inertia is computed: $I_{tot,upperleg} = 6.02 \cdot 10^{-2} kg\ m^2$. Through the superposition of the effects the upperleg inertia is derived as: $I_{upperleg} = I_{tot,upperleg} - 2I_{gear} = 5.93 \cdot 10^{-2} kg\ m^2$.

From equation (3.29), the hip shaft bearings friction coefficient c_{hip} is computed: $c_{hip} = 1.67 \cdot 10^{-2} Nm\ s$.

3.3.4 Lowerleg

The lowerleg mass is measured with a weight scale, it results to be $m_{lowleg} = 0.61kg$. The center of mass is computed measuring the knee torque. The lowerleg is placed horizontally and the measured torque is divided by the subsystem weight force. The torque is $T_{lowerleg} = 0.6Nm$ and the center of mass is $L_{cm,lowerleg} = \dfrac{T_{lowerleg}}{m_{lowerleg}\ g} = 0.10m$.

From the free oscillations shown in Figure 3.29, the parameter δ is computed accordingly to equation (3.30) and the frequency f is measured. The resulting values are $\delta = 0.13$ and $f = 1.13Hz$. Therefore, the natural frequency and and the damping factor are derived as stated in equations (3.31-3.32): $w_n = 7.08 rad/s$ and $\zeta = 2.50 \cdot 10^{-3}$.

By means of equation (3.28), the lowerleg inertia is computed: $I_{lowerleg} = 1.20 \cdot 10^{-2} kg\ m^2$.

From equation (3.29), the knee shaft bearings friction coefficient c_{knee} is computed: $c_{knee} = 4.23 \cdot 10^{-4} Nm\ s$.

The lowerleg gear bearings friction coefficient is computed connecting the tendons to the lowerleg and removing the worm gear in order to let the total system oscillate freely. The total mass is computed as $m_{tot,lowerleg} = m_{lowerleg} + m_{tendons} + m_{gear} = 1.38kg$.
The new center of mass is computed through the superposition of the effects similarly to

Figure 3.29: Lowerleg free oscillations

equation (3.33): $L_{cm,tot} = \dfrac{L_{cm,lowerleg}\ m_{lowerleg}}{m_{tot,lowerleg}} = 4.43 \cdot 10^{-2}$.

Again, from the free oscillations shown in Figure 3.30, the parameter δ is computed accordingly to equation (3.30) and the frequency f is measured. The resulting values are $\delta = 0.27$ and $f = 1.10Hz$. Therefore, the natural frequency and and the damping factor are derived as stated in equations (3.31-3.32): $w_n = 6.91rad/s$ and $\zeta = 1.20 \cdot 10^{-2}$.

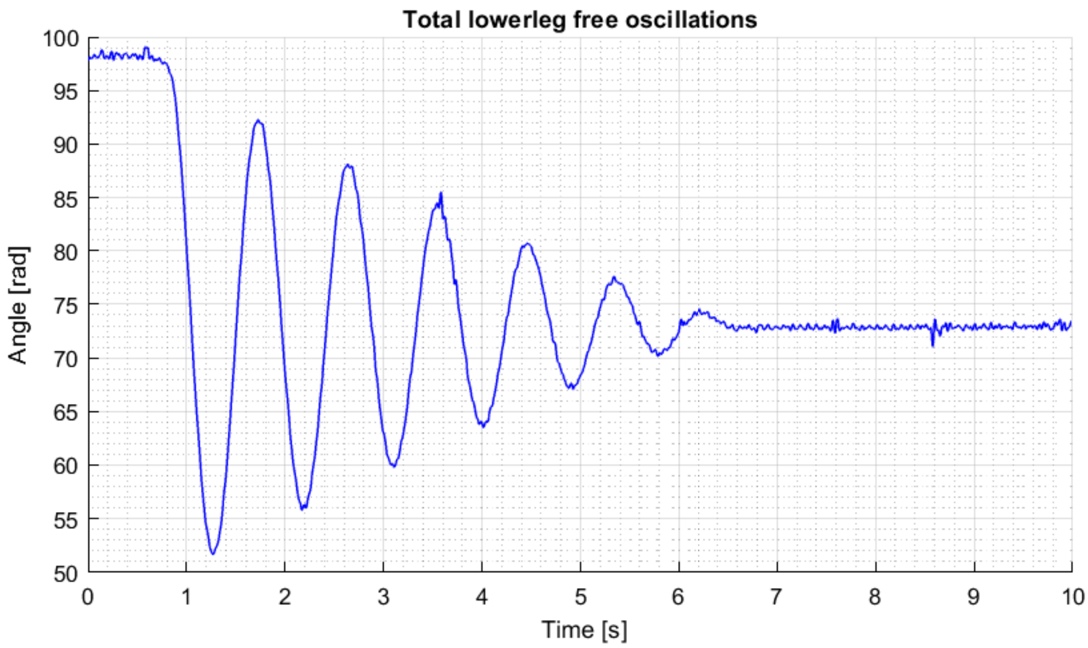

Figure 3.30: Total lowerleg free oscillations

By means of equation (3.28), the total subsystem inertia is computed: $I_{tot,lowerleg} = 1.26 \cdot 10^{-2} kg\ m^2$. As expected, the difference of inertia between the lowerleg and the total lowerleg subsystems corresponds to the gear one and to the contribution due to the tendons moving: $\Delta I = I_{gear} + 2m_{tendon}\ r_{tendon}$. With r_{tendon} the projection of the fixing point of the tendons to the knee shaft along the flexible link plane.

From equation (3.29), the total friction coefficient c_{tot}, corresponding to the sum of the contributions of the knee shaft bearings and the gear bearings friction, is computed: $c_{tot} = 2.08 \cdot 10^{-3} Nm\ s$. The gear bearings friction coefficient is derived as $c_{gear} = c_{tot} - c_{knee} = 1.66 \cdot 10^{-3} Nm\ s$.

3.4 Encoder acquisition

The encoders provide the absolute angle position as PWM-encoded output signal. In the producer datasheet it is stated that one PWM clock period represents 0.088 degree and it has a typical duration of 444 ns. The output signal consists of a frame of 4119 PWM clock periods. The output signal frequency results to be around $f_{PWM} = 547Hz$. This leads to a constraint on the sampling frequency of the control system code: $f_s < f_{PWM}$.

Since the encoder voltage signal is proportional to the joint angle, the scale factor was identified by rotating each joint of a known angle and measuring the resulting voltage variation.
The output signal is affected by a noise of $0.2rad$ of pick to pick amplitude and about $f_{noise} = \frac{1}{3} f_s$ of frequency. This makes the angle readings too noisy to be used in a control loop. Therefore a low pass filter is designed and added after the signal reading.
Chosen a sampling frequency of $f_s = 400Hz$, the noise frequency results to be around $f_{noise} = 133Hz$.
In order to attenuate the noise magnitude of 60 dB and to get a usable signal for a control action, a fourth order low pass filter is designed. It is composed by two second order Butterworth low pass filters with cut-off frequency of $25Hz$.
The encoder signal filter transfer function is:

$$G_{filter}(s) = \left(\frac{1}{1 + \frac{1.414s}{25} + \left(\frac{s}{25}\right)^2} \right)^2 \tag{3.34}$$

The bode diagram of the encoder signal filter is shown in Figure 3.31.

The cleaning action of the filter is shown in Figure 3.32 where a joint is moved of $0.3rad$ at different frequencies and the raw angle measure is plotted against the filtered one.

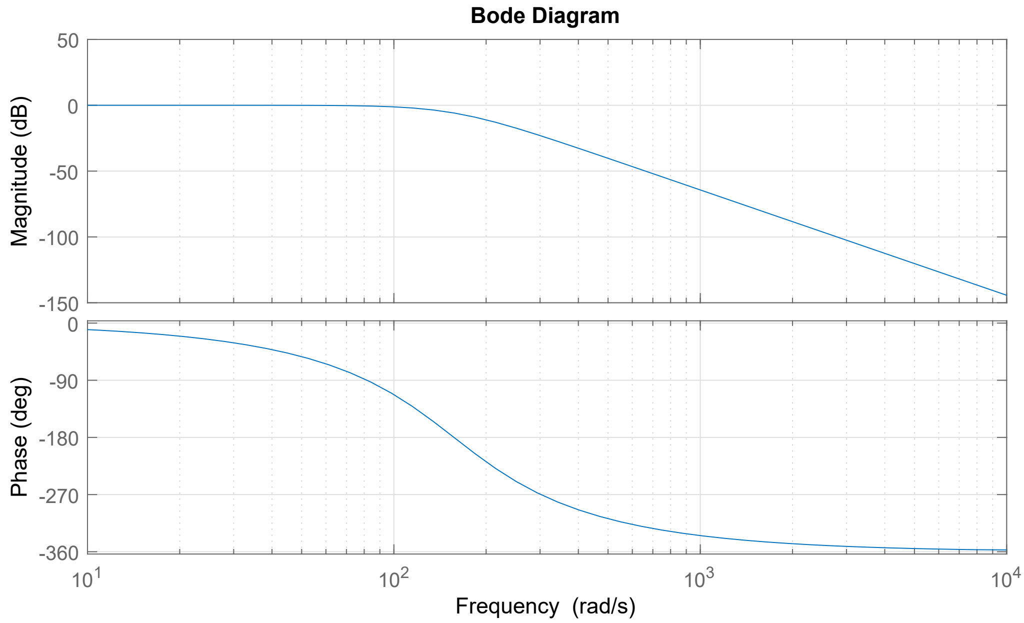

Figure 3.31: Encoder signal filter bode diagram

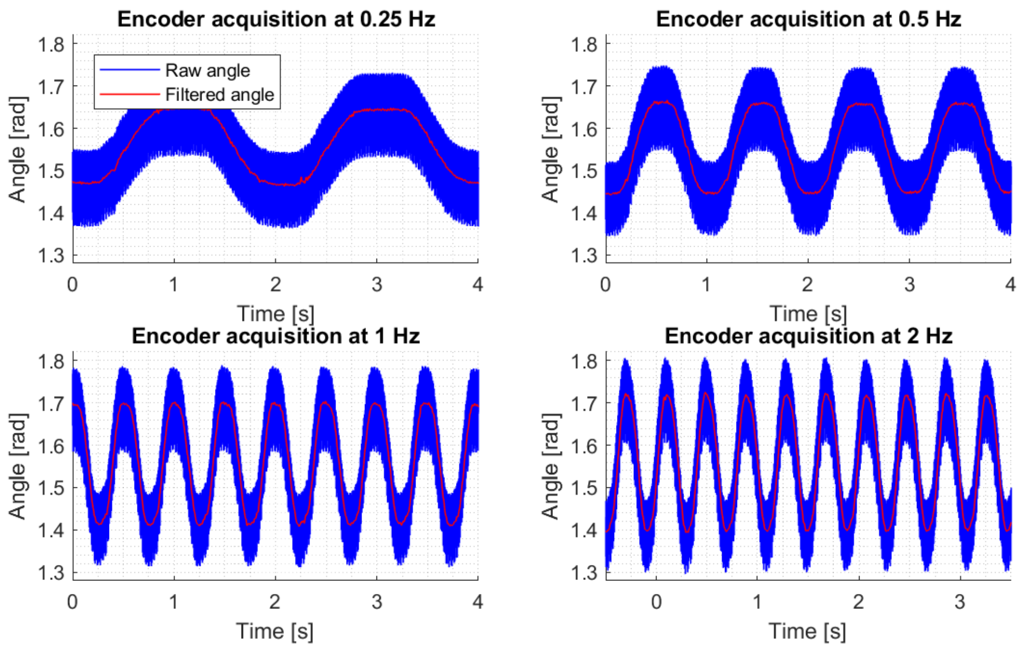

Figure 3.32: Encoder signal filter action

Chapter 4

Mathematical model

The mathematical model of the leg, described in [17], can be written as in equation 4.1.

$$M(\boldsymbol{q})\,\ddot{\boldsymbol{q}} + h(\boldsymbol{q}, \dot{\boldsymbol{q}}) + G(\boldsymbol{q}) = \tau \tag{4.1}$$

This model is highly non-linear and coupled, this makes hard the control algorithm design. However, under the assumptions that the joint velocity is slow and that the mass is concentrated mostly on the linear guide, the term containing Coriolis and centrifugal forces $h(\boldsymbol{q}, \dot{\boldsymbol{q}})$ can be neglected and the mass matrix can be considered constant. In addition, the gravity force can be compensated in feed-forward, so that the Eq.4.1 can be decoupled.
Another approximation, that can be done in order to derive a first model for the joint angle control design, is that both the links are rigid, since the lowerleg deformation is negligible with respect to its movement due to the motors action.
Taking into account these assumptions, it is possible to derive the transfer functions describing the motion of the upper and lower link both in the flying and the stance phases.
After the system characterization procedure, the only parameter which remains uncertain is the friction proper of the wormgear system. This because the mechanical structure prevents to perform meaningful measurements.
In order to derive the transfer function of lower and upper link in both the phases, the bond graph technique is used.

4.1 Coordinate reference frames

With the coordinate reference frames depicted in Figure 4.1, the joint angles are defined as:

θ_1 : hip joint angle, the rotation around the z axis of the hip joint reference frame $\Re_1$ with respect to the world reference frame $\Re_0$. This is the angle measured by the hip encoder and actuated by the hip motor.

θ_2 : knee joint angle, the rotation around the z axis of the knee joint reference frame $\Re_2$ with respect to the hip joint reference frame $\Re_1$. This is the angle measured by the knee encoder.

$\theta_2 + \theta_1$: absolute knee joint angle, the rotation around the z axis of the knee joint reference frame $\Re_2$ with respect to the world reference frame $\Re_0$. This is the angle actuated by the knee motor.

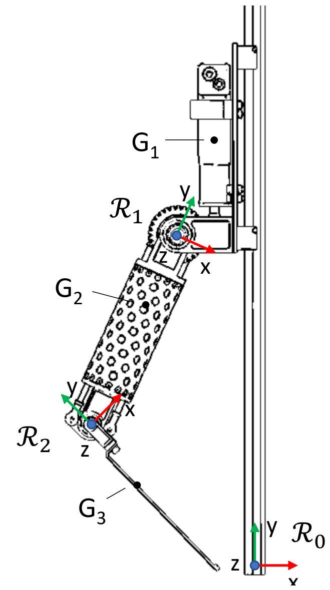

Figure 4.1: FlegX reference frames

4.2 Flight phase

4.2.1 Lowerleg

In flight phase, the bond graph model shown in Figure 4.2 is used for modelling the lowerleg subsystem.
Since the motor is driven in torque control, it can be considered as source of effort.

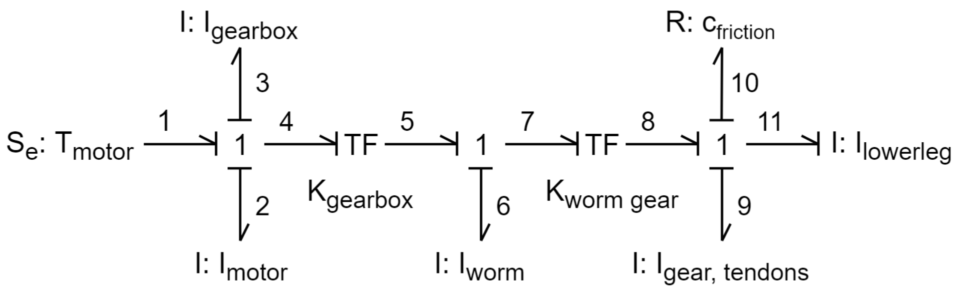

Figure 4.2: Flight phase lowerleg bond graph model

With:

T_{motor} : the torque produced by the motor

I_{motor} : the motor shaft inertia with respect to its rotation axis

$I_{gearbox}$: the gearbox inertia with respect to its rotation axis

$K_{gearbox}$: the gearbox transform ratio

I_{worm} : the worm gear inertia with respect to its rotation axis

$K_{worm\ gear}$: the worm gear transform ratio

$c_{friction}$: the lowerleg friction coefficient

$I_{gear,\ tendons}$: the gear and the tendons inertia with respect to the gear rotation axis

$I_{lowerleg}$: the lowerleg inertia with respect to the joint axis

The speed of the shaft on which the knee encoder is placed is the f_{11}. Therefore the measured angle is

$$\begin{aligned} \theta(t) &= \int f_{11}(t)dt \\ f_{11} &= \frac{1}{I_{lowerleg}} \int e_{11}(t)dt \end{aligned} \tag{4.2}$$

The equations for each component are derived according to the scheme depicted in Figure 4.2.

$$\begin{aligned}
e_1 &= T_m & f_1 &= f_4 \\
e_2 &= I_{motor}\frac{df_2}{dt} & f_2 &= f_4 \\
e_3 &= I_{gearbox}\frac{df_3}{dt} & f_3 &= f_4 \\
e_4 &= e_1 - e_2 - e_3 & f_4 &= K_{gearbox} f_5 \\
e_5 &= K_{gearbox} e_4 & f_5 &= f_7 \\
e_6 &= I_{worm}\frac{df_6}{dt} & f_6 &= f_7 \\
e_7 &= e_5 - e_6 & f_7 &= K_{worm\ gear} f_8 \\
e_8 &= K_{worm\ gear} e_7 & f_8 &= f_{11} \\
e_9 &= c_{friction} f_9 & f_9 &= f_{11} \\
e_{10} &= I_{gear,\ tendons}\frac{df_{10}}{dt} & f_{10} &= f_{11} \\
e_{11} &= e_8 - e_9 - e_{10} & \frac{df_{11}}{dt} &= \frac{1}{I_{lowerleg}} e_{11}
\end{aligned}$$

Defining

$$\begin{aligned} K_{eq\ motor} &= \frac{I_{motor} + I_{gearbox}}{I_{lowerleg}} \left(K_{gearbox} K_{worm\ gear}\right)^2 \\ K_{eq\ worm} &= \frac{I_{worm}}{I_{lowerleg}} K^2_{worm\ gear} \\ K_{eq\ gear} &= \frac{I_{gear,\ tendons}}{I_{lowerleg}} \end{aligned} \tag{4.3}$$

The effort e_{11} results to be

$$e_{11}(t) = \frac{K_{gearbox} K_{worm\ gear}}{1 + K_{eq\ motor} + K_{eq\ worm} + K_{eq\ gear}} T_{motor}(t) - \frac{c_{friction}}{I_{lowerleg}} \int e_{11}(t)dt \tag{4.4}$$

By applying to equation (4.4) the Laplace transform, the transfer function between the torque e_{11} and the input torque T_{motor} is computed.

$$\frac{e_{11}(s)}{T_{motor}(s)} = \frac{\dfrac{K_{gearbox} K_{worm\ gear}}{1 + K_{eq\ motor} + K_{eq\ worm} + K_{eq\ gear}}}{1 + \dfrac{c_{friction}}{I_{lowerleg}} \dfrac{1}{s}} \tag{4.5}$$

Taking into account the relation (4.2), from equation (4.5), the transfer function between the measured angle θ and the input torque T_{motor} is derived.

$$\frac{\theta(s)}{T_{motor}(s)} = \frac{1}{s} \frac{\dfrac{\dfrac{K_{gearbox}K_{worm\ gear}}{1 + K_{eq\ motor} + K_{eq\ worm} + K_{eq\ gear}}}{I_{lowerleg}}}{s + \dfrac{c_{friction}}{I_{lowerleg}}} \tag{4.6}$$

The transfer function between the absolute knee joint angle $(\theta_2 + \theta_1)$ and the input torque is computed taking into account the lowerleg subsystem parameters.

$$\frac{\theta_2(s) + \theta_1(s)}{T_{motor}(s)} = \frac{1}{s} \frac{176.76}{s + \dfrac{c_{knee\ friction}}{1.20\ 10^{-2}}} \tag{4.7}$$

In the derived transfer function the friction parameter is only in part known, during the control design phase its contribution is studied.

4.2.2 Upperleg

The upperleg subsystem in flight mode is derived taking into account as lowerleg a fixed link positioned in a medium operating angle $\theta_{knee} = \dfrac{\pi}{4}$. The model shown in Figure 4.3 is used for modelling the upperleg subsystem.
As for the previously analyzed case, since the motor is driven in torque control, it can be considered as source of effort.

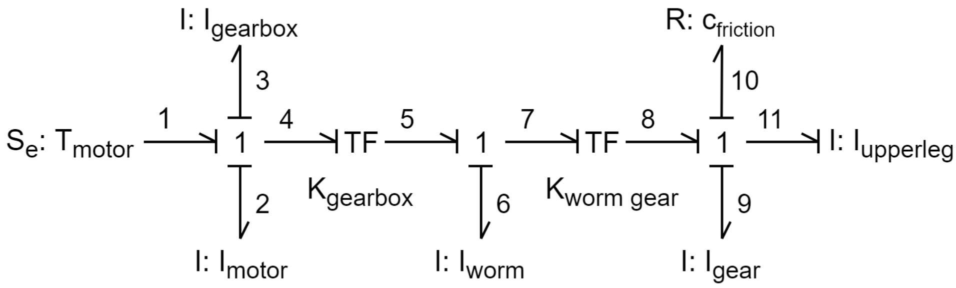

Figure 4.3: Flight phase upperleg bond graph model

With:

$c_{friction}$: the upperleg friction coefficient

I_{gear} : the gear inertia with respect to its rotation axis

$I_{upperleg}$: the upperleg inertia with respect to the joint axis, taking into account the lowerleg as a point mass positioned in its center of mass

The speed of the shaft on which the knee encoder is placed is the f_{11}. Therefore the measured angle is

$$\theta(t) = \int f_{11}(t)dt$$
$$f_{11} = \frac{1}{I_{upperleg}} \int e_{11}(t)dt \tag{4.8}$$

The equations for each component are derived according to the scheme depicted in Figure 4.3.

$$
\begin{aligned}
&e_1 = T_m && f_1 = f_4\\
&e_2 = I_{motor}\frac{df_2}{dt} && f_2 = f_4\\
&e_3 = I_{gearbox}\frac{df_3}{dt} && f_3 = f_4\\
&e_4 = e_1 - e_2 - e_3 && f_4 = K_{gearbox} f_5\\
&e_5 = K_{gearbox} e_4 && f_5 = f_7\\
&e_6 = I_{worm}\frac{df_6}{dt} && f_6 = f_7\\
&e_7 = e_5 - e_6 && f_7 = K_{worm\ gear} f_8\\
&e_8 = K_{worm\ gear} e_7 && f_8 = f_{11}\\
&e_9 = c_{friction} f_9 && f_9 = f_{11}\\
&e_{10} = I_{gear}\frac{df_{10}}{dt} && f_{10} = f_{11}\\
&e_{11} = e_8 - e_9 - e_{10} && \frac{df_{11}}{dt} = \frac{1}{I_{upperleg}} e_{11}
\end{aligned}
$$

Defining

$$
\begin{aligned}
K_{eq\ motor} &= \frac{I_{motor} + I_{gearbox}}{I_{upperleg}} \left(K_{gearbox} K_{worm\ gear}\right)^2\\
K_{eq\ worm} &= \frac{I_{worm}}{I_{upperleg}} K^2_{worm\ gear}\\
K_{eq\ gear} &= \frac{I_{gear}}{I_{upperleg}}
\end{aligned}
\tag{4.9}
$$

The effort e_{11} results to be

$$
e_{11}(t) = \frac{K_{gearbox} K_{worm\ gear}}{1 + K_{eq\ motor} + K_{eq\ worm} + K_{eq\ gear}} T_{motor}(t) - \frac{c_{friction}}{I_{upperleg}} \int e_{11}(t) dt \tag{4.10}
$$

By applying the Laplace transform to the effort equation and by exploiting the angle-torque relation described in (4.8), the transfer function between the measured angle (θ) and the input torque is derived.

$$
\frac{\theta(s)}{T_{motor}(s)} = \frac{1}{s} \frac{\dfrac{\dfrac{K_{gearbox} K_{worm\ gear}}{1 + K_{eq\ motor} + K_{eq\ worm} + K_{eq\ gear}}}{I_{upperleg}}}{s + \dfrac{c_{friction}}{I_{upperleg}}} \tag{4.11}
$$

Therefore, the transfer function between the hip joint angle (θ_1) and the input torque is computed.

$$
\frac{\theta_1(s)}{T_{motor}(s)} = \frac{1}{s} \frac{162.12}{s + \dfrac{c_{knee\ friction}}{1.43\ 10^{-1}}} \tag{4.12}
$$

As for the lowerleg subsystem, in the upperleg transfer function, the friction parameter is only in part known, during the control design phase its contribution is studied.

4.3 Stance phase

In order to take into account the motors and the support inertia, it is necessary to find the relation between their speed and the joint velocities.

From the reference frame scheme depicted in Figure 4.1, the motors and support center of mass G_1 pose is computed as function of the joint angles.

$$p_{G_1} = \begin{bmatrix} -k_x \\ L\cos(\theta_2+\theta_1) + L\cos\theta_1 + k_y \\ 0 \end{bmatrix} \tag{4.13}$$

With

L : the upperleg and the lowerleg length (equal by construction)

k_x : the horizontal distance between the motors and support center of mass from the linear guide

k_y : the vertical distance between the motors and support center of mass and the hip joint ($\Re_1$)

The motors and support speed is computed by deriving (4.13).

$$\dot{p}_{G_1} = \begin{bmatrix} 0 \\ -L\sin(\theta_2+\theta_1) \\ 0 \end{bmatrix} \left(\dot{\theta}_2 + \dot{\theta}_1\right) + \begin{bmatrix} 0 \\ -L\sin(\theta_1) \\ 0 \end{bmatrix} \left(\dot{\theta}_1\right) \tag{4.14}$$

The joint speeds must have a precise relation so that the leg does not slip on the floor. Such a constraint is found by computing the lowerleg tip pose and, deriving it, imposing the horizontal speed equal to zero.
As for the motors and support center of mass, the tip pose is computed as function of the joint angles.

$$p_{tip} = \begin{bmatrix} -k'_x + L\sin\theta_1 + L\sin(\theta_2+\theta_1) \\ 0 \\ 0 \end{bmatrix} \tag{4.15}$$

With k'_x the horizontal distance of the hip joint from the linear guide.

In order to generate at the hip shaft only a vertical force and to avoid undesired torques, the leg is constrained to touch the ground at the vertical projection of the hip rotation axis: $p_{tip,\ x} = -k'_x + L\sin\theta_1 + L\sin(\theta_2+\theta_1) = -k'_x$.
This leads to a simple relation between the joint angles.

$$\theta_2 = -2\theta_1 \tag{4.16}$$

The tip speed is computed by deriving (4.15).

$$\dot{p}_{tip} = \begin{bmatrix} L\cos\theta_1\dot{\theta}_1 + L\cos(\theta_2+\theta_1)\left(\dot{\theta}_2+\dot{\theta}_1\right) \\ 0 \\ 0 \end{bmatrix} \tag{4.17}$$

Imposing the horizontal speed equal to zero and taking into account (4.16), the relation between the joint velocities is found.

$$\dot{\theta}_2 = -2\dot{\theta}_1 \tag{4.18}$$

If the joints perform small movements, it is possible to linearise the speed stated in (4.14) around $\theta_1 = -\theta_0$ and $\theta_2 = 2\theta_0$.

$$\dot{p}_{G_1} = -L \sin\theta_0 \dot{\theta}_2 \tag{4.19}$$

Equation (4.19) shows a relation between the motors and support center of mass vertical speed and the knee joint velocity. Taking into account (4.18) and the symmetry of the sin function ($\sin\theta = \sin(-\theta)$), the relation between the motors and support center of mass vertical speed and the hip joint velocity is found.

$$\dot{p}_{G_1} = 2L \sin\theta_0 \dot{\theta}_1 \tag{4.20}$$

Combining the results (4.20) and (4.19), the relation between the motors and support center of mass vertical speed and the absolute knee joint velocity ($\dot{\theta}_2 + \dot{\theta}_1$) is found.

$$\dot{p}_{G_1} = -2L \sin\theta_0 (\dot{\theta}_2 + \dot{\theta}_1) \tag{4.21}$$

By means of the superposition of the effects, taking into account one torque at a time, the relation between the inertia force of the motors and support plate and the joint torques is computed.
Starting from the hip joint torque (considering the knee joint torque null), the lowerleg can transmit only an axial force generated by the the motors and support inertia subject to an acceleration a. The joints are considered in the linearisation angles position.

$$F_{lowerleg} = \frac{m_{motors\ support} a}{\cos\theta_0} \tag{4.22}$$

The hip torque can therefore be computed as

$$T_1 = F_{lowerleg} \cos\left(\frac{\pi}{2} - 2\theta_0\right) = 2L \sin\theta_0 m_{motors\ support} a \tag{4.23}$$

While the knee torque is computed considering the hip joint torque null, the only force the the upperleg can transmit is an axial one, it is computed again as in (4.22). Therefore, the knee torque is computed as in (4.23) but with the negative sign.

$$T_2 = -2L \sin\theta_0 m_{motors\ support} a \tag{4.24}$$

The relations stated in (4.20, 4.23) and (4.21, 4.24) are modelled in the bond graph environment as transformers with a ratio of $\pm 2L \sin\theta_0$.

4.3.1 Lowerleg

The bond graph model shown in Figure 4.4 is used for modelling the lowerleg subsystems.

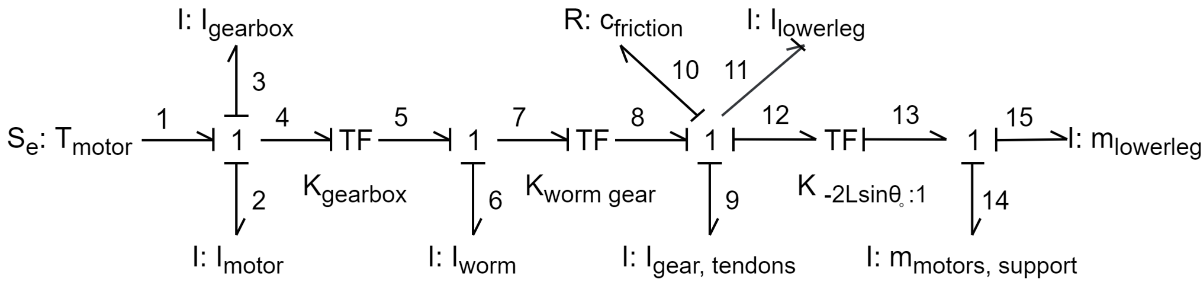

Figure 4.4: Stance phase lowerleg bond graph model

With, in addiction to the flight case model, the following parameters:

$K_{-2L\sin\theta_0:1}$: the transformer ratio between the motor and support speed and the absolute knee joint velocity $(\dot{\theta}_2 + \dot{\theta}_1)$

$m_{motors,\ support}$: the mass of the motor and support plate

$m_{lowerleg}$: the sum of the lowerleg and upperleg masses

The speed of the shaft on which the encoder is placed is, as in the flight phase, the f_{11}. Therefore the measured angle is

$$\begin{aligned} \theta(t) &= \int f_{11}(t)dt \\ f_{11} &= \frac{1}{I_{lowerleg}} \int e_{11}(t)dt \end{aligned} \tag{4.25}$$

The equations for each component are derived according to the scheme depicted in Figure 4.4.

$$\begin{aligned}
e_1 &= T_m & f_1 &= f_4 \\
e_2 &= I_{motor}\frac{df_2}{dt} & f_2 &= f_4 \\
e_3 &= I_{gearbox}\frac{df_3}{dt} & f_3 &= f_4 \\
e_4 &= e_1 - e_2 - e_3 & f_4 &= K_{gearbox} f_5 \\
e_5 &= K_{gearbox} e_4 & f_5 &= f_7 \\
e_6 &= I_{worm}\frac{df_6}{dt} & f_6 &= f_7 \\
e_7 &= e_5 - e_6 & f_7 &= K_{worm\ gear} f_8 \\
e_8 &= K_{worm\ gear} e_7 & f_8 &= f_{11} \\
e_9 &= c_{friction} f_9 & f_9 &= f_{11} \\
e_{10} &= I_{gear,\ tendons}\frac{df_{10}}{dt} & f_{10} &= f_{11} \\
e_{11} &= e_8 - e_9 - e_{10} & \frac{df_{11}}{dt} &= \frac{1}{I_{lowerleg}} e_{11} \\
e_{12} &= -2L\sin\theta_0 e_{13} & f_{12} &= f_{11} \\
e_{14} &= m_{motors,\ support}\frac{df_{14}}{dt} & f_{14} &= -2L\sin\theta_0 f_{12} \\
e_{15} &= m_{lowerleg}\frac{df_{15}}{dt} & f_{15} &= f_{14}
\end{aligned}$$

Adding to the definitions stated in (4.3)

$$K_{eq\ support} = \frac{m_{motors,\ support} + m_{lowerleg}}{I_{lowerleg}} (-2L\sin\theta_0)^2 \tag{4.26}$$

The effort e_{11} results to be

$$e_{11}(t) = \frac{K_{gearbox} K_{worm\ gear}}{1 + K_{eq\ motor} + K_{eq\ worm} + K_{eq\ gear} + K_{eq\ support}} T_{motor}(t) - \frac{c_{friction}}{I_{lowerleg}} \int e_{11}(t) dt \tag{4.27}$$

By applying to equation (4.27) the Laplace transform, the transfer function between the torque e_{11} and the input torque T_{motor} is computed.

$$\frac{e_{11}(s)}{T_{motor}(s)} = \frac{\dfrac{K_{gearbox} K_{worm\ gear}}{1 + K_{eq\ motor} + K_{eq\ worm} + K_{eq\ gear} + K_{eq\ support}}}{1 + \dfrac{c_{friction}}{I_{lowerleg}} \dfrac{1}{s}} \tag{4.28}$$

Taking into account the relation (4.25), from equation (4.28), the transfer function between the measured angle θ and the input torque T_{motor} is derived.

$$\frac{\theta(s)}{T_{motor}(s)} = \frac{1}{s} \frac{\dfrac{\dfrac{K_{gearbox} K_{worm\ gear}}{1 + K_{eq\ motor} + K_{eq\ worm} + K_{eq\ gear} + K_{eq\ support}}}{I_{lowerleg}}}{s + \dfrac{c_{friction}}{I_{lowerleg}}} \tag{4.29}$$

As example, the transfer function between the absolute knee joint angle $(\theta_2 + \theta_1)$ and the input torque is computed with a linearisation angle $\theta_0 = \dfrac{\pi}{6}$.

$$\frac{\theta_2(s) + \theta_1(s)}{T_{motor}(s)} = \frac{1}{s} \frac{108.36}{s + \dfrac{c_{knee\ friction}}{1.20\ 10^{-2}}} \tag{4.30}$$

As for the flight phase, the friction parameter is only in part known. Its contribution is studied during the control design phase.

4.3.2 Upperleg

The upperleg subsystem is modelled with the bond graph model shown in Figure 4.4.

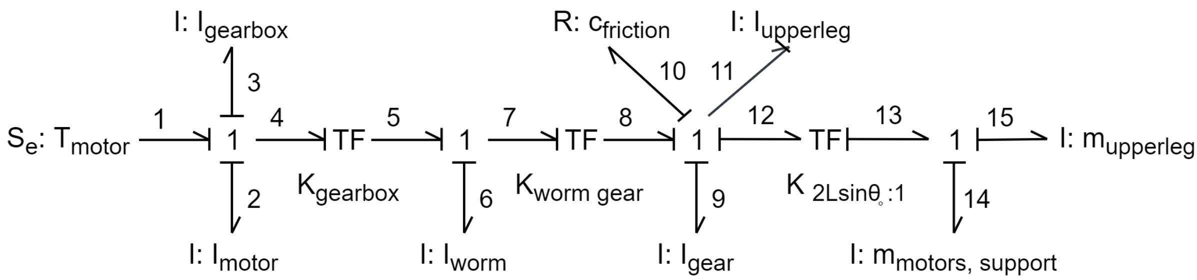

Figure 4.5: Stance phase upperleg bond graph model

With, in addiction to the upperleg flight phase model, the following parameters:

$K_{2L\sin\theta_0:1}$: the transformer ratio between the motor and support speed and the hip joint velocity $(\dot{\theta}_1)$

$m_{upperleg}$: the upperleg mass

The speed of the shaft on which the encoder is placed is, as in the flight phase, the f_{11}. Therefore the measured angle is

$$\begin{aligned} \theta(t) &= \int f_{11}(t)dt \\ f_{11} &= \frac{1}{I_{lowerleg}} \int e_{11}(t)dt \end{aligned} \tag{4.31}$$

The equations for each component are derived according to the scheme depicted in Figure 4.4.

$$\begin{aligned}
e_1 &= T_m & f_1 &= f_4 \\
e_2 &= I_{motor}\frac{df_2}{dt} & f_2 &= f_4 \\
e_3 &= I_{gearbox}\frac{df_3}{dt} & f_3 &= f_4 \\
e_4 &= e_1 - e_2 - e_3 & f_4 &= K_{gearbox} f_5 \\
e_5 &= K_{gearbox} e_4 & f_5 &= f_7 \\
e_6 &= I_{worm}\frac{df_6}{dt} & f_6 &= f_7 \\
e_7 &= e_5 - e_6 & f_7 &= K_{worm\ gear} f_8 \\
e_8 &= K_{worm\ gear} e_7 & f_8 &= f_{11} \\
e_9 &= c_{friction} f_9 & f_9 &= f_{11} \\
e_{10} &= I_{gear}\frac{df_{10}}{dt} & f_{10} &= f_{11} \\
e_{11} &= e_8 - e_9 - e_{10} & \frac{df_{11}}{dt} &= \frac{1}{I_{upperleg}} e_{11} \\
e_{12} &= 2L\sin\theta_0 e_{13} & f_{12} &= f_{11} \\
e_{14} &= m_{motors,\ support}\frac{df_{14}}{dt} & f_{14} &= 2L\sin\theta_0 f_{12} \\
e_{15} &= m_{upperleg}\frac{df_{15}}{dt} & f_{15} &= f_{14}
\end{aligned}$$

Defining

$$K_{eq\ support} = \frac{m_{motors,\ support} + m_{upperleg}}{I_{upperleg}} (2L\sin\theta_0)^2 \tag{4.32}$$

The effort e_{11} results to be

$$e_{11}(t) = \frac{K_{gearbox}K_{worm\ gear}}{1 + K_{eq\ motor} + K_{eq\ worm} + K_{eq\ gear} + K_{eq\ support}} T_{motor}(t) - \frac{c_{friction}}{I_{upperleg}} \int e_{11}(t)dt \tag{4.33}$$

By applying the Laplace transform and taking into account the relation (4.31), the transfer function between the measured angle θ and the input torque T_{motor} is derived.

$$\frac{\theta(s)}{T_{motor}(s)} = \frac{1}{s} \frac{\dfrac{\dfrac{K_{gearbox}K_{worm\ gear}}{1 + K_{eq\ motor} + K_{eq\ worm} + K_{eq\ gear} + K_{eq\ support}}}{I_{upperleg}}}{s + \dfrac{c_{friction}}{I_{upperleg}}} \tag{4.34}$$

Again, as example, the transfer function between the hip joint angle (θ_1) and the input torque is computed with a linearisation angle $\theta_0 = \dfrac{\pi}{6}$.

$$\frac{\theta_1(s)}{T_{motor}(s)} = \frac{1}{s} \frac{106.24}{s + \dfrac{c_{hip\ friction}}{1.43\ 10^{-1}}} \tag{4.35}$$

As for the flight phase, the friction parameter is only in part known and its contribution is studied during the control design phase.

4.4 Motor model

Since it is not possible to get a model of the motors driver with the current control, it has been decided to identify the system "driver + motor" (duty cycle - current) and to use it as black box model, as shown in Figure 4.6.

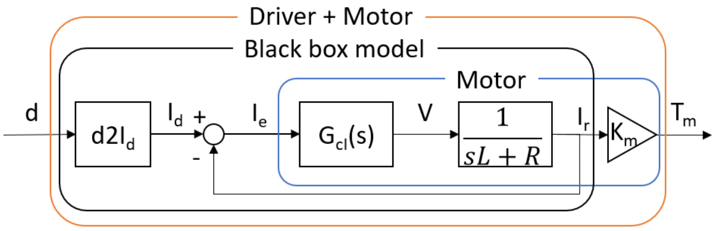

Figure 4.6: Motor model

The a-priori information are:

- The driver controller should be a PI, it has 1 pole
- The electrical circuit has 1 pole due to the motor inductance

Therefore, a second order function has been chosen as system model.

Different square waves signals have been used as input to the driver and the corresponding current measurements have been acquired through Escon Studio. The collected data is shown in Figure 4.7.

Imported the data in Matlab, the system identification tool has been used.
The mean value (50) has been removed from the input signal, while the output one has already zero mean value.
The final chosen model has 1 zero and 2 poles:

$$\frac{I(s)}{d(s)} = \frac{0.20\left(1+\dfrac{s}{4403}\right)}{\left(1+\dfrac{s}{1.61\ 10^6}\right)\left(1+\dfrac{s}{4201}\right)} \tag{4.36}$$

The simulation results obtained through the identified model are compared to the acquired ones on Figure 4.8.

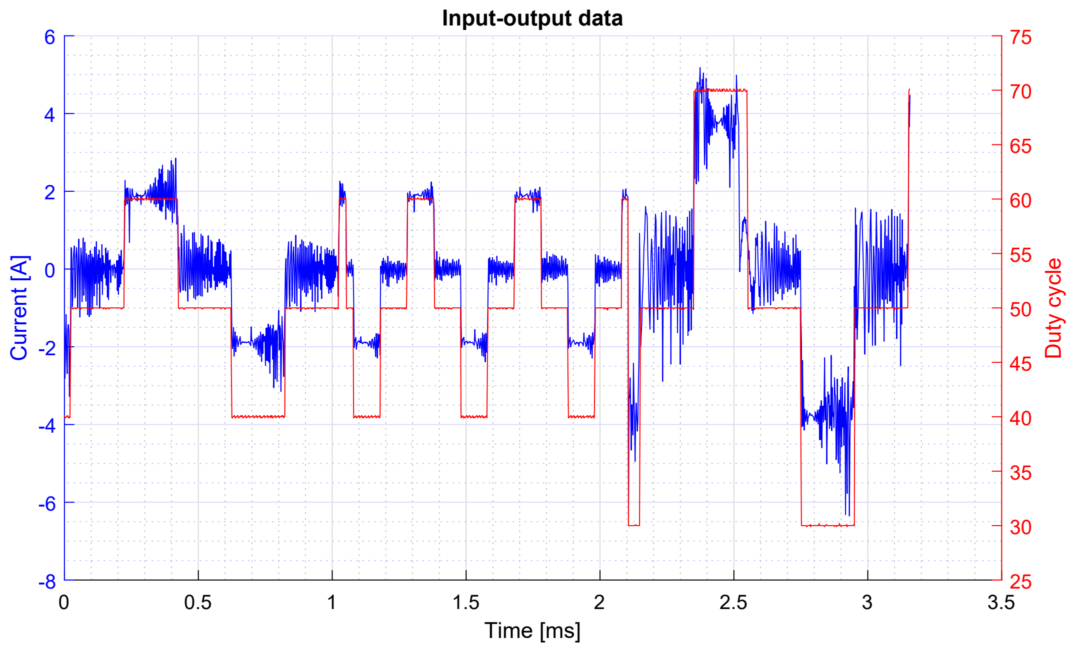

Figure 4.7: Motor current response to square wave duty cycle signals

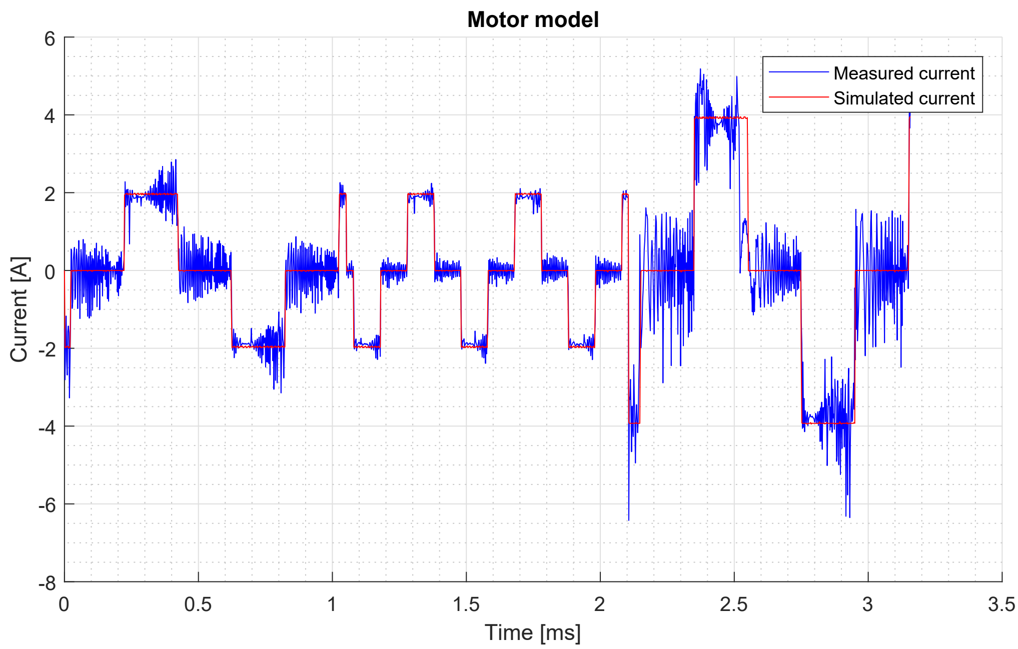

Figure 4.8: Motor data simulation compared to acquired motor data

4.5 Closed loop model

The overall closed loop model is completed with the torque constant $K_m = 42.7mNm/A$ stated into the motors datasheets and the encoder filter in the feedback loop as shown in Figure 4.9.

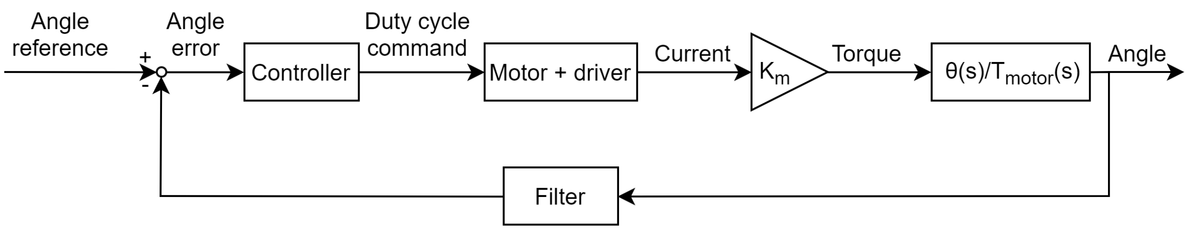

Figure 4.9: Closed loop model

Chapter 5

Controller design

The dynamics of a robotic leg can be described through the hybrid dynamic system theory [18, 19]. The model is composed by one discrete state σ, which describes the phases of the jump, and a vector of infinite continuous states describing the dynamics of the flexible structure in the different conditions. The hybrid dynamic system model is shown in Figure 5.1.

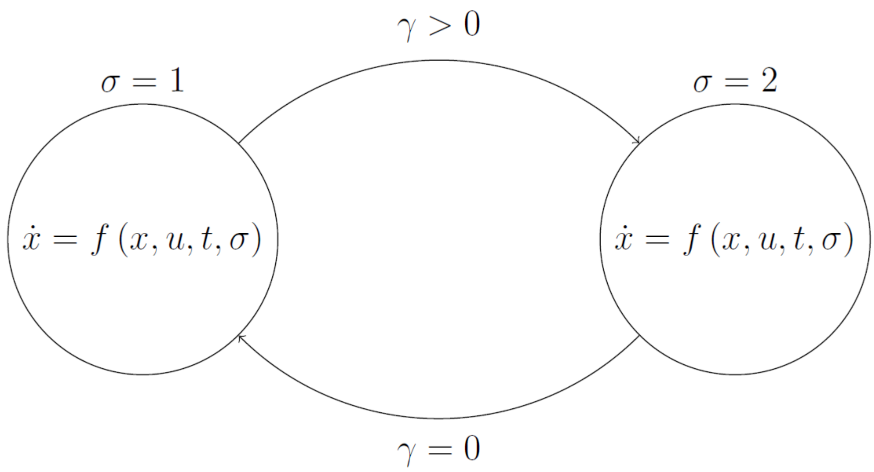

Figure 5.1: Hybrid dynamic system model

In Figure 5.1, the discrete parameter σ identifies the leg phase, either $\sigma = 1$ if the leg is in the stance one or $\sigma = 2$ if it is in the flight one. The transition between this two phases is described by the boolean variable γ, this is detected though either the flexible link strain gauge readings or the knee torque sensor ones. For the two phases the equations derived in chapter 4 are used.
This family of dynamic systems is characterised by discontinuities in the differential equations during the transition between a discrete state to another. In rigid robotic legs the transition between the flight phase and the stance one produces a jump discontinuity in the joint velocity, this phenomenon may lead the system to instability. The introduction of a flexible link in the leg mechanism can be a solution to this problem. The compliance of this structural element acts like a filter, cutting the high frequency dynamics caused by the impulsive force induced by the impact between the leg and the ground. It allows to move the discontinuity from the joint velocity to state variables related to the vibrational

dynamics of the flexible element.

The most common controller used in this type of system is the PD controller with a feed-forward term used to compensate the gravity. However, this type of controller is very sensitive to noise, so, to avoid this problem, the control law proposed is based on a phase-lead network.

5.1 Gravity compensation

Since the leg models have been derived without taking into account the gravity effect, its contribution is compensated through a feed-forward term, as shown in Figure 5.2.

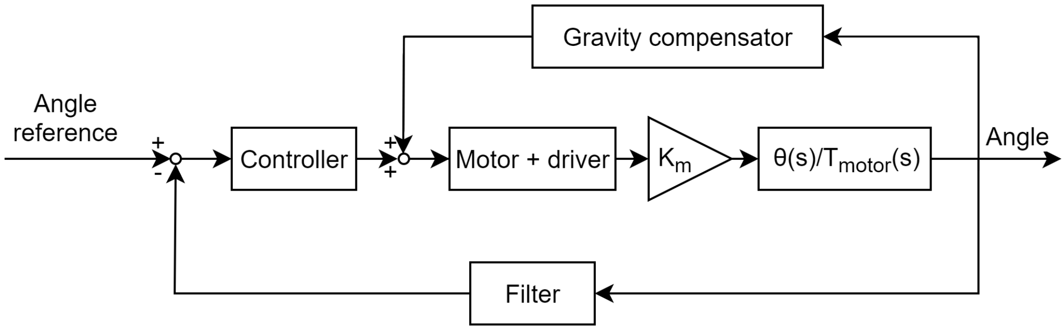

Figure 5.2: Gravity compensated system model

The gravitational force generated by the mass of each component produces different torques at the two rotational joints depending on the leg phase.
From the virtual work (δW) computation, the relation between the joint torques and the virtual forces ($\mathcal{F}$) is computed. The hip torque is called T_{hip}, the knee one T_{knee}, the hip angle θ_{hip} and the measured (relative) knee angle θ_{knee}.

$$\delta W = \mathcal{F}_1 \delta\theta_{hip} + \mathcal{F}_2 \delta\theta_{knee} = T_{hip}\delta\theta_{hip} + T_{knee}(\delta\theta_{hip} + \delta\theta_{knee}) \tag{5.1}$$

This brings to the joint torques computation as follows.

$$\begin{aligned} T_{hip} &= \mathcal{F}_1 - \mathcal{F}_2 \\ T_{knee} &= \mathcal{F}_2 \end{aligned} \tag{5.2}$$

5.1.1 Flight phase

During the flight phase, the two joints have to counteract only the weight force due to the components connected after them: the knee joint has to balance the lowerleg force and the kip joint the two links one. The relations between the two virtual forces and the joint angles are derived from the leg geometrical analysis.

$$\begin{aligned} \mathcal{F}_1 &= m_{ll} g \; l_{cm,ll} \sin(\theta_{hip} + \theta_{knee}) + (m_{ul} \; l_{cm,ul} + m_{ll} \; L_{ul}) g \sin(\theta_{hip}) \\ \mathcal{F}_2 &= m_{ll} g \; l_{cm,ll} \sin(\theta_{hip} + \theta_{knee} \end{aligned} \tag{5.3}$$

With

m_{ll} and m_{ul}: the lowerleg and upperleg masses

$l_{cm,ll}$ and $l_{cm,ul}$: the lowerleg and upperleg center of mass distances from the knee and hip joints respectively

L_{ul}: the rigid link length

$$\begin{aligned} \mathcal{F}_1 &= 0.60\sin(\theta_{hip} + \theta_{knee}) + 4.26\sin(\theta_{hip}) \\ \mathcal{F}_2 &= 0.60\sin(\theta_{hip} + \theta_{knee}) \end{aligned} \tag{5.4}$$

By taking into account equations (5.2) and (5.4), the joint torques needed to balance the weight force in flight mode are computed.

$$\begin{aligned} T_{hip} &= 4.26\sin(\theta_{hip}) \\ T_{knee} &= 0.60\sin(\theta_{hip} + \theta_{knee}) \end{aligned} \tag{5.5}$$

5.1.2 Stance phase

In stance phase, the two joints have to counteract the weight force due to the components connected before them, where the major contribution is given by the leg support along with the motors. The relations between the two virtual forces and the joint angles are derived from the leg geometrical analysis.

$$\begin{aligned} \mathcal{F}_1 = \quad & -(m_{supp}L_{ul} + m_{ul}L_{ul} + m_{ll}(L_{ll} - l_{cm,ll}))g\sin(\theta_{hip} + \theta_{knee}) + \\ & -(m_{supp}L_{ul} + m_{ul}(L_{ul} - l_{cm,ul}))g\sin(\theta_{hip}) \\ \mathcal{F}_2 = \quad & -m_{supp}L_{ul} + m_{ul}L_{ul} + m_{ll}(L_{ll} - l_{cm,ll}))g\sin(\theta_{hip} + \theta_{knee}) \end{aligned} \tag{5.6}$$

With

m_{supp}: the support plate and motors masses

m_{ll} and m_{ul}: the lowerleg and upperleg masses

$l_{cm,ll}$ and $l_{cm,ul}$: the lowerleg and upperleg center of mass distances from the knee and hip joints respectively

L_{ll} and L_{ul}: the flexible and rigid link lengths

$$\begin{aligned} \mathcal{F}_1 &= -29.24\sin(\theta_{hip} + \theta_{knee}) - 25.59\sin(\theta_{hip}) \\ \mathcal{F}_2 &= -29.24\sin(\theta_{hip} + \theta_{knee}) \end{aligned} \tag{5.7}$$

By taking into account equations (5.2) and (5.7), the joint torques needed to balance the weight force in stance mode are computed.

$$\begin{aligned} T_{hip} &= -25.59\sin(\theta_{hip}) \\ T_{knee} &= -29.24\sin(\theta_{hip} + \theta_{knee}) \end{aligned} \tag{5.8}$$

5.2 Loop shaping controller design

Since the leg is modelled as an hybrid dynamic system defined by two different discrete states, it needs two different control laws, one for each phase.
The proposed analysis starts evaluating the mathematical models derived in chapter 4 with as friction only the bearings one computed in section 3.3. Then, the friction parameter is varied and the closed loop system behaviour is analyzed in order to find how the controller should be modified in order to keep the desired performances.

5.2.1 Flight phase

Lowerleg

Adding the bearing friction information in the mathematical model derived in section 4.2, the transfer function for the lowerleg in flight phase is computed.

$$\frac{\theta_2(s)+\theta_1(s)}{T_{motor}(s)} = \frac{1}{s}\frac{176.76}{s+0.17} \tag{5.9}$$

Referring to the generic closed loop system model shown in Figure 5.3, the direct branch G is computed as function of the unknown lowerleg flight phase controller function $G_{c,ll,f}$.

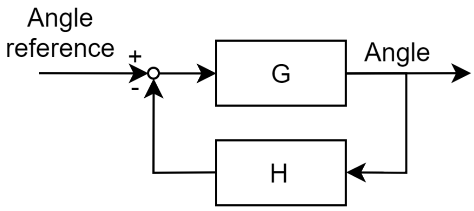

Figure 5.3: Generic closed loop system model

$$G(s) = G_{c,ll,f}(s)\frac{1.14\ 10^7(s+4403)}{s(s+1.16\ 10^6)(s+4201)(s+0.17)} \tag{5.10}$$

The feedback branch H is composed by the encoder filter function stated in section 3.4.

$$H(s) = \left(\frac{1}{1+\frac{1.414s}{25}+\left(\frac{s}{25}\right)^2}\right)^2 \tag{5.11}$$

Since the encoder filter introduces a fast phase lag, the proposed controller is based on a phase-lead action. The controller is designed trying to shape the closed loop function like a prototype second order function on the Nychols chart. The used prototype is slightly under-damped, in order to have a fast response ($\zeta = 0.6$), with the crossover frequency as fast as possible.

$$G_{c,ll,f}(s) = \frac{1.4(s+0.18)}{1+\frac{s}{50}} \tag{5.12}$$

As shown in Figure 5.4, the obtained closed loop function has a gain crossover frequency of $\omega_{cp} = 10.17\ rad/s$, a phase crossover frequency of $\omega_{cg} = 45.45\ rad/s$ and a phase margin of $\varphi_m = 68.06\,\text{deg}$.

The computed controller is suitable for the considered function but the real leg has the power transmission system friction that is unknown. Increasing the friction parameter, in order to keep the loop shape unchanged, it is necessary to increase only the controller zero frequency proportionally. Therefore, this parameter has to be tuned experimentally. An example is shown in Figure 5.5, where the friction parameter has been increased ten times and the controller zero has been modified to keep the loop shape as the one obtained during the controller design process.

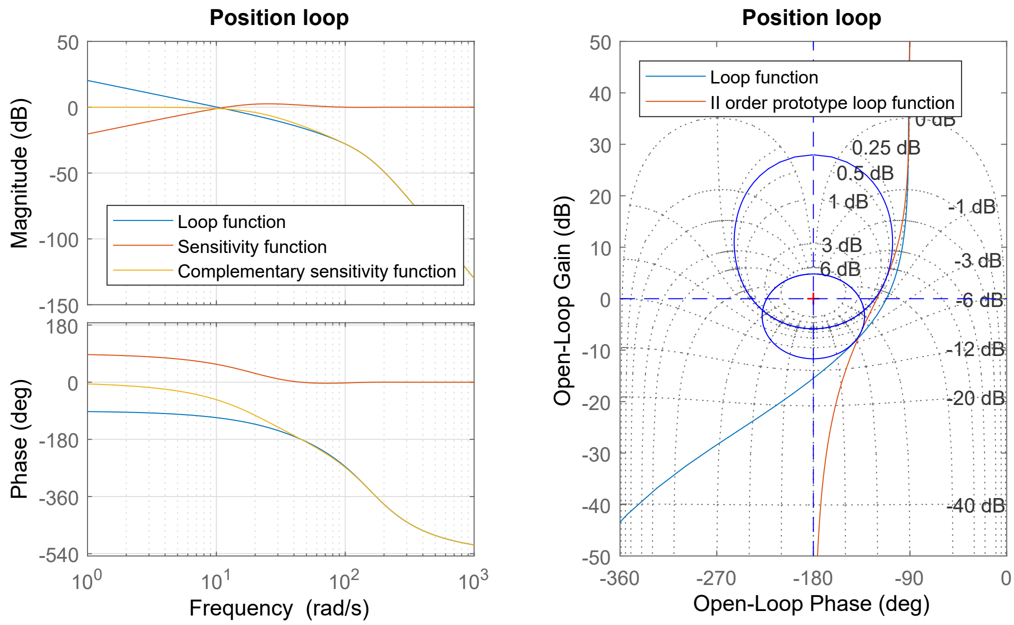

Figure 5.4: Lowerleg flight phase closed loop Bode diagram and Nichols chart

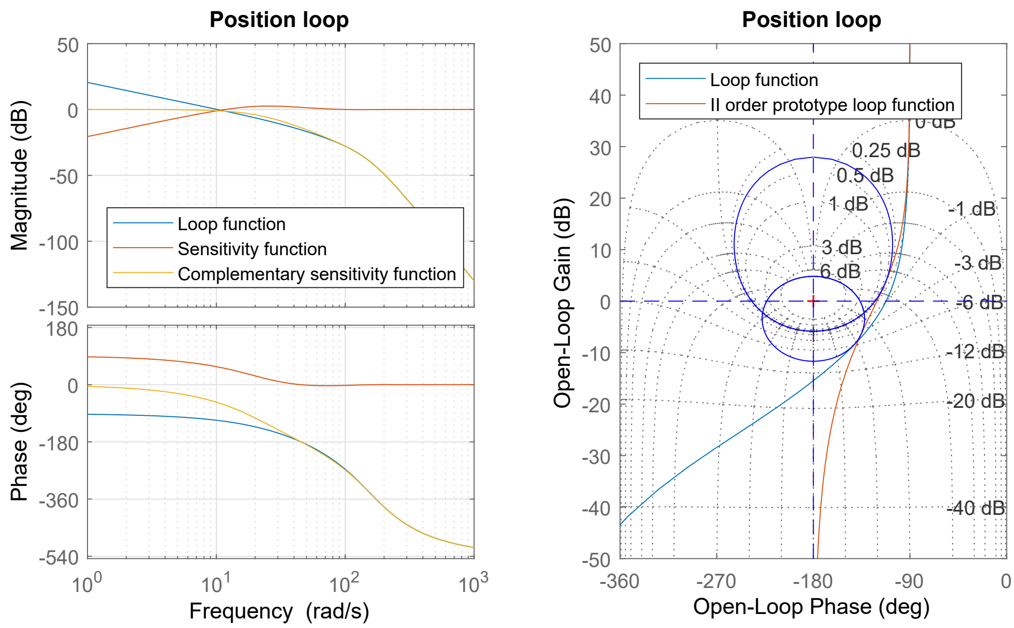

Figure 5.5: Modified lowerleg flight phase closed loop Bode diagram and Nichols chart

The modified controller is $G_{c,ll,f,mod}(s) = \dfrac{1.4(s+1.8)}{1+\dfrac{s}{50}}$.

The final result obtained from the experimental tuning operation, compared to the model simulation, is discussed in chapter 6.

Upperleg

From the mathematical model derived in section 4.2, the transfer function for the upperleg in flight phase is computed adding the bearing friction information.

$$\frac{\theta_1(s)}{T_{motor}(s)} = \frac{1}{s}\frac{162.12}{s+0.28} \tag{5.13}$$

Referring to the generic closed loop system model shown in Figure 5.3, the direct branch G is computed in function of the unknown upperleg flight phase controller function $G_{c,ul,f}$.

$$G(s) = G_{c,ul,f}(s)\frac{1.05\ 10^7(s+4403)}{s(s+1.16\ 10^6)(s+4201)(s+0.28)} \tag{5.14}$$

The feedback branch H is composed by the encoder filter function stated in section 3.4.

$$H(s) = \left(\frac{1}{1+\dfrac{1.414s}{25}+\left(\dfrac{s}{25}\right)^2}\right)^2 \tag{5.15}$$

As for the lowerleg, since the encoder filter introduces a fast phase lag, the proposed controller is based on a phase-lead action. The controller is designed trying to shape the closed loop function like a prototype second order function on the Nychols chart. The used prototype is slightly under-damped, in order to have a fast response ($\zeta = 0.6$), with the crossover frequency as fast as possible.

$$G_{c,ul,f}(s) = \frac{1.4(s+0.12)}{1+\dfrac{s}{40}} \tag{5.16}$$

As shown in Figure 5.6, the obtained closed loop function has a gain crossover frequency of $\omega_{cp} = 9.28\ rad/s$, a phase crossover frequency of $\omega_{cg} = 67.25\ rad/s$ and a phase margin of $\varphi_m = 70.48\,\text{deg}$.

Again, since the real leg has the power transmission system friction that is unknown, the computed controller is suitable only for the considered function. Increasing the friction parameter, in order to keep the loop shape unchanged, it is necessary to increase the controller zero frequency proportionally. Therefore, as for the lowerleg controller, this parameter has to be tuned experimentally. An example is shown in Figure 5.7, where the friction parameter has been increased ten times and the controller zero has been modified to keep the loop shape as the one obtained during the controller design process.

The modified controller is $G_{c,ul,f,mod}(s) = \dfrac{1.4(s+1.2)}{1+\dfrac{s}{40}}$.

The final result obtained from the experimental tuning operation, compared to the model simulation, is discussed in chapter 6.

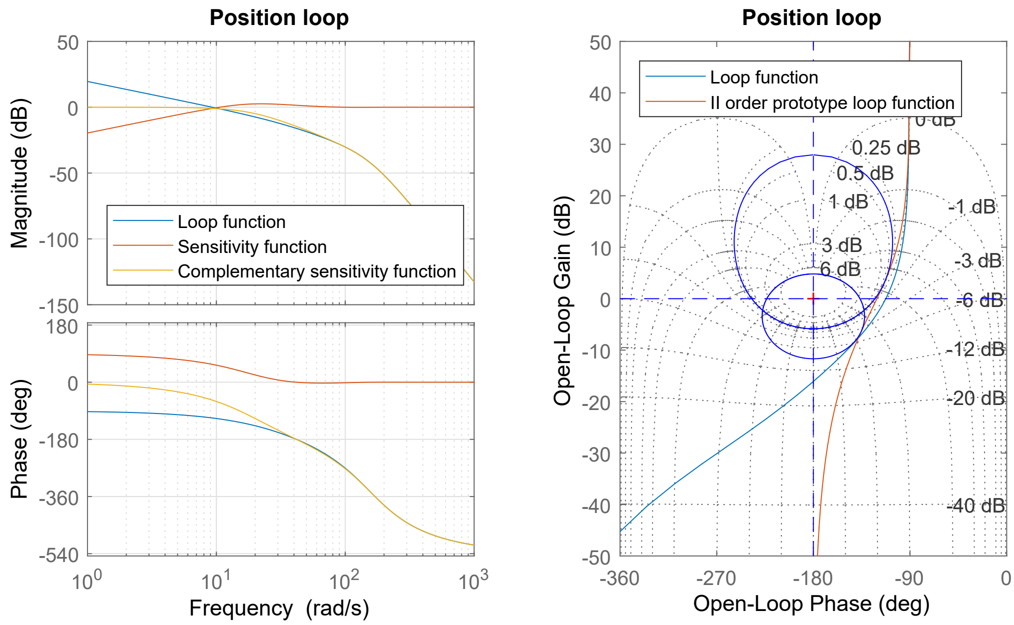

Figure 5.6: Upperleg flight phase closed loop Bode diagram and Nichols chart

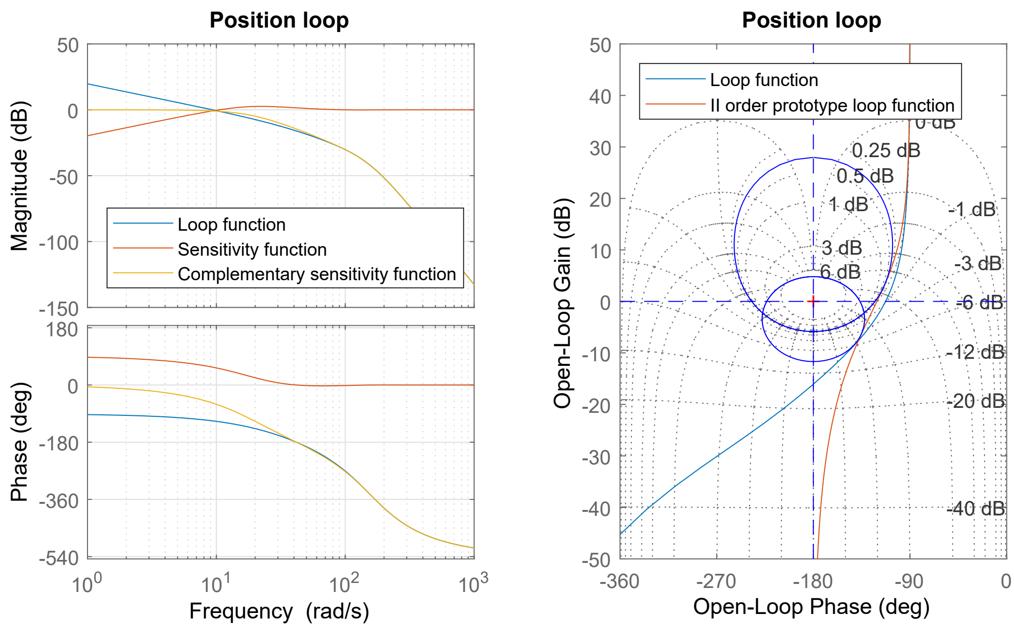

Figure 5.7: Modified upperleg flight phase closed loop Bode diagram and Nichols chart

5.2.2 Stance phase

The same procedure used for the flight phase is followed to find a suitable controller for the stance phase.

Lowerleg

Starting from the mathematical model derived in section 4.3, the transfer function for the lowerleg in stance phase is computed adding the bearing friction information.

$$\frac{\theta_2(s)+\theta_1(s)}{T_{motor}(s)} = \frac{1}{s}\frac{108.36}{s+0.17} \tag{5.17}$$

Referring to the generic closed loop system model shown in Figure 5.3, the direct branch G is computed in function of the unknown lowerleg flight phase controller function $G_{c,ll,s}$.

$$G(s) = G_{c,ll,s}(s)\frac{6.99\ 10^6(s+4403)}{s(s+1.16\ 10^6)(s+4201)(s+0.17)} \tag{5.18}$$

The feedback branch H is composed by the encoder filter function stated in section 3.4.

$$H(s) = \left(\frac{1}{1+\frac{1.414s}{25}+\left(\frac{s}{25}\right)^2}\right)^2 \tag{5.19}$$

Due to the fast phase lag introduced by the filtering action, the proposed controller is based on a phase-lead action. The controller is designed trying to shape the closed loop function like a prototype second order function on the Nychols chart. The used prototype is slightly under-damped, in order to have a fast response ($\zeta = 0.6$), with the crossover frequency as fast as possible.

$$G_{c,ll,s}(s) = \frac{2.4(s+0.18)}{1+\frac{s}{50}} \tag{5.20}$$

As shown in Figure 5.8, the obtained closed loop function has a gain crossover frequency of $\omega_{cp} = 10.67\ rad/s$, a phase crossover frequency of $\omega_{cg} = 45.45\ rad/s$ and a phase margin of $\varphi_m = 67.00\,\text{deg}$.

The obtained controller is effective only for the analyzed model, but the real one has an higher dissipative component due to the power transmission system. Increasing the friction parameter, in order to keep the loop shape unchanged, it is necessary to increase the controller zero frequency proportionally. Therefore, as for the flight phase, this parameter has to be tuned experimentally. An example is shown in Figure 5.9, where the friction parameter has been increased ten times and the controller zero has been modified to keep the loop shape as the one obtained during the controller design process.

The modified controller is $G_{c,ll,s,mod}(s) = \dfrac{2.4(s+1.8)}{1+\frac{s}{50}}$.

The final result obtained from the experimental tuning operation, compared to the model simulation, is discussed in chapter 6.

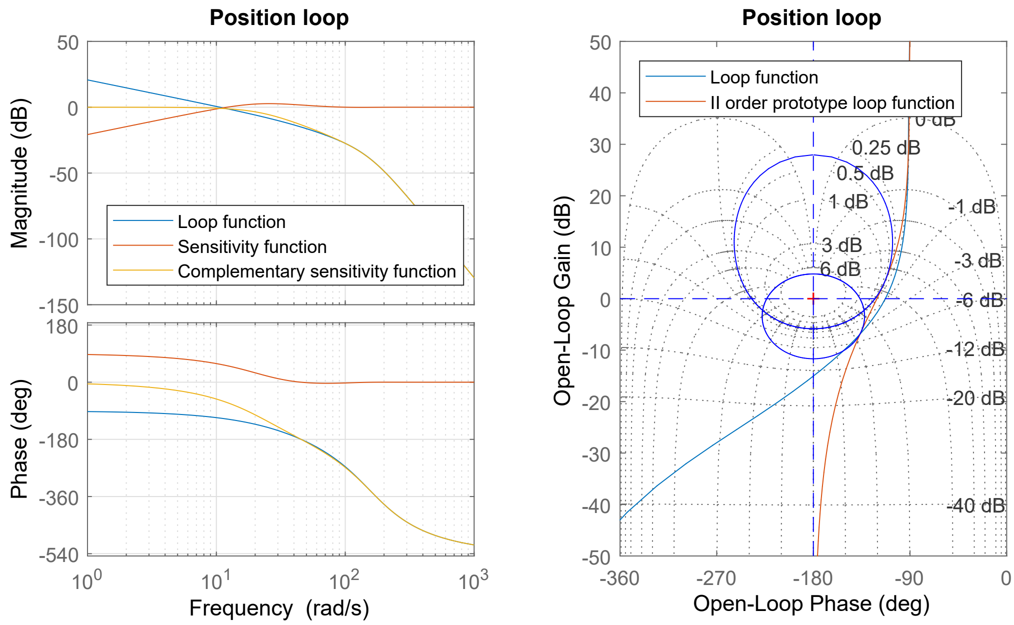

Figure 5.8: Lowerleg stance phase closed loop Bode diagram and Nichols chart

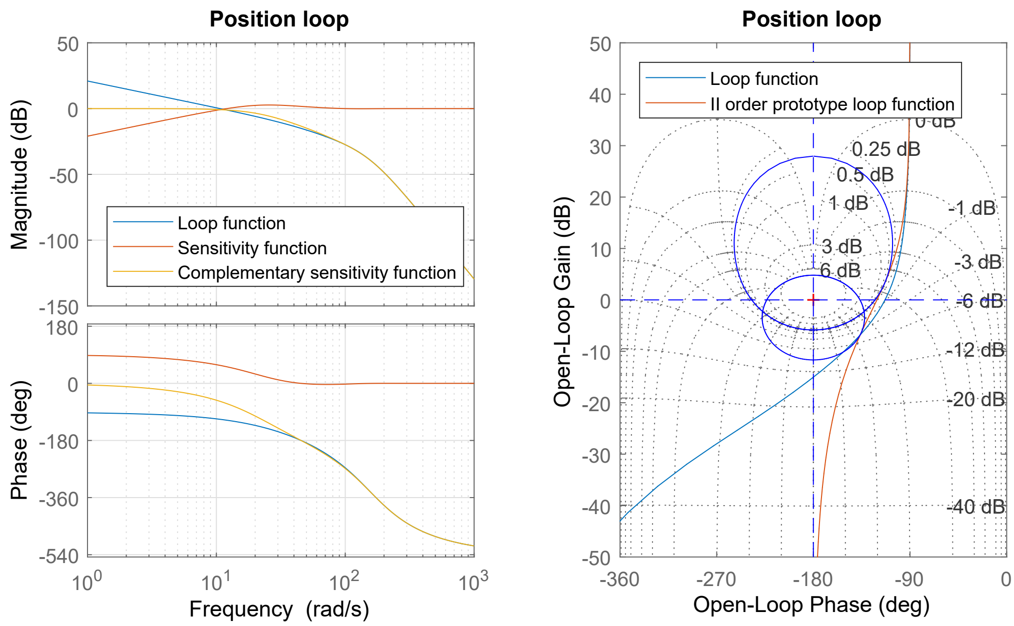

Figure 5.9: Modified lowerleg stance phase closed loop Bode diagram and Nichols chart

Upperleg

From the mathematical model derived in section 4.3, the transfer function for the upperleg in stance phase is computed adding the bearing friction information.

$$\frac{\theta_1(s)}{T_{motor}(s)} = \frac{1}{s}\frac{106.24}{s+0.28} \tag{5.21}$$

Referring to the generic closed loop system model shown in Figure 5.3, the direct branch

G is computed in function of the unknown upperleg flight phase controller function $G_{c,ul,f}$.

$$G(s) = G_{c,ul,s}(s)\frac{6.85\ 10^6(s + 4403)}{s(s + 1.16\ 10^6)(s + 4201)(s + 0.28)} \tag{5.22}$$

The feedback branch H is composed by the encoder filter function stated in section 3.4.

$$H(s) = \left(\frac{1}{1 + \frac{1.414s}{25} + \left(\frac{s}{25}\right)^2}\right)^2 \tag{5.23}$$

As for the lowerleg, since the encoder filter introduces a fast phase lag, the proposed controller is based on a phase-lead action. The controller is designed trying to shape the closed loop function like a prototype second order function on the Nychols chart. The used prototype is slightly under-damped, in order to have a fast response ($\zeta = 0.6$), with the crossover frequency as fast as possible.

$$G_{c,ul,s}(s) = \frac{2.2(s + 0.3)}{1 + \frac{s}{40}} \tag{5.24}$$

As shown in Figure 5.10, the obtained closed loop function has a gain crossover frequency of $\omega_{cp} = 9.58\ rad/s$, a phase crossover frequency of $\omega_{cg} = 65.75\ rad/s$ and a phase margin of $\varphi_m = 69.54\,\text{deg}$.

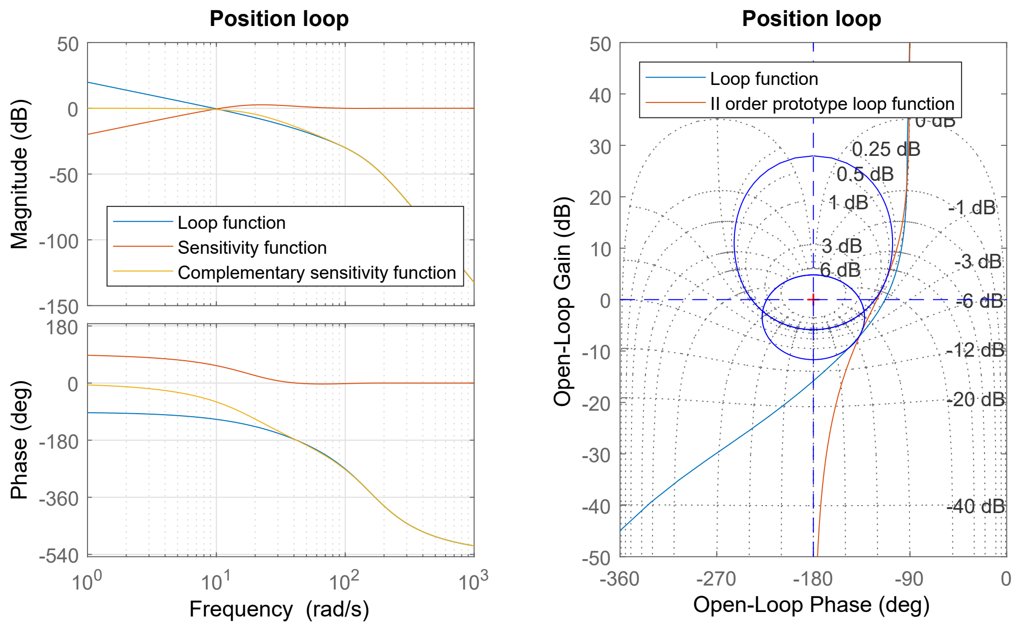

Figure 5.10: Upperleg stance phase closed loop Bode diagram and Nichols chart

Again, since the real leg has the power transmission system friction that is unknown, the computed controller is effective only for the considered function. Increasing the friction parameter, in order to keep the loop shape unchanged, it is necessary to increase the controller zero frequency proportionally. Therefore, as for the flight phase, this parameter has to be tuned experimentally. An example is shown in Figure 5.11, where the friction parameter has been increased ten times and the controller zero has been modified to keep the loop shape as the one obtained during the controller design process.

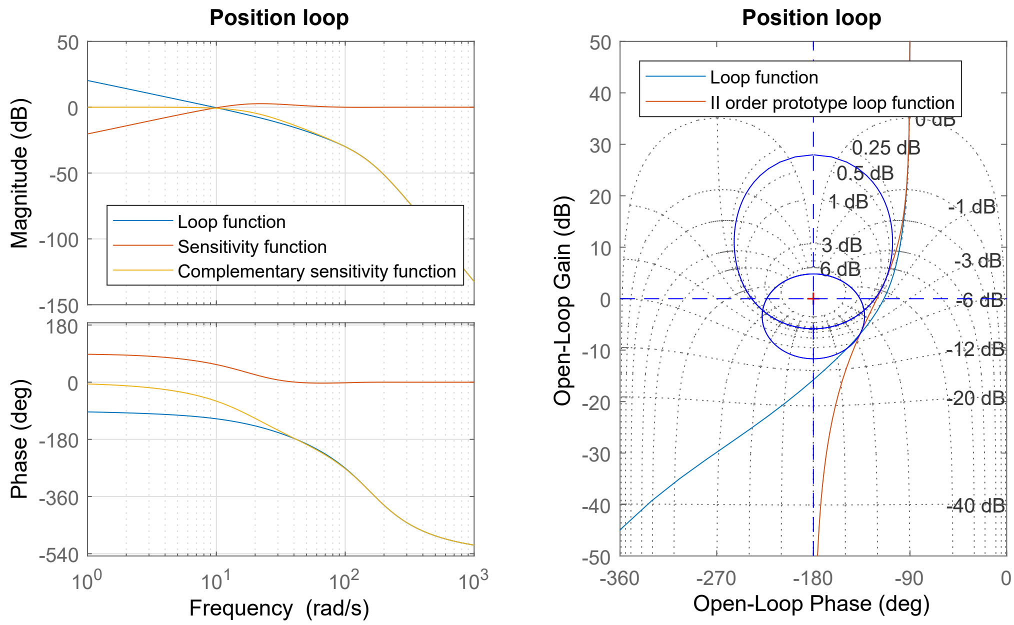

Figure 5.11: Modified upperleg stance phase closed loop Bode diagram and Nichols chart

The modified controller is $G_{c,ul,s}(s) = \dfrac{2.2(s+3.0)}{1+\dfrac{s}{40}}$.

The final result obtained from the experimental tuning operation, compared to the model simulation, is discussed in chapter 6.

Chapter 6

Experimental results

6.1 Controller tuning

The four controllers are tuned by applying to each subsystem some angle references signals. For the proposed tests, the input command is composed by repeating sequences of fifth order splines between two angular positions with a period of $T_r = 0.7s$, in order to generate a signal frequency slightly lower than the crossover one proper of the controllers.

6.1.1 Flight phase

The leg is hanged on the linear guide suspended in order to let it move freely.

Lowerleg

Since the encoder measures the relative knee angle θ_2 and the motor torque actuates the absolute one $\theta_2 + \theta_1$, the input reference is computed by subtracting from the spline signal the hip angle θ_1. The requested reference amplitude is about 20 deg, from 90 deg to 70 deg and its frequency around $1.43Hz$. The controller zero is increased till the system response becomes comparable to the simulation one, the final controller function is:

$$G_{c,ll,f}(s) = \frac{1.5(s + 2.5)}{1 + \frac{s}{50}} \tag{6.1}$$

The measured response is compared with the simulation one in Figure 6.1.

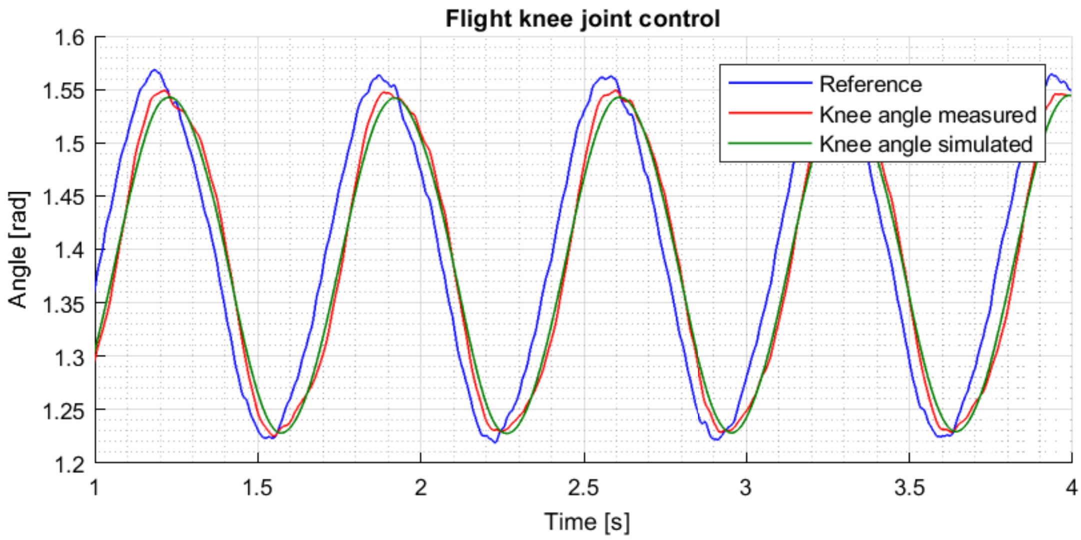

Figure 6.1: Lowerleg flight phase response

Upperleg

The input reference is directly computed with the spline signal. Its amplitude is about 10 deg, from −40 deg to −50 deg, half with respect to the lowerleg one in order to keep the linearisation condition used during the mathematical model derivation in chapter 4. The signal frequency is kept, as for the lowerleg, around $1.43Hz$. The controller zero is increased till the system response becomes comparable to the simulation one, the final controller function is:

$$G_{c,ll,f}(s) = \frac{1.6(s+2.5)}{1+\dfrac{s}{40}} \tag{6.2}$$

The measured response is compared with the simulation one in Figure 6.2.

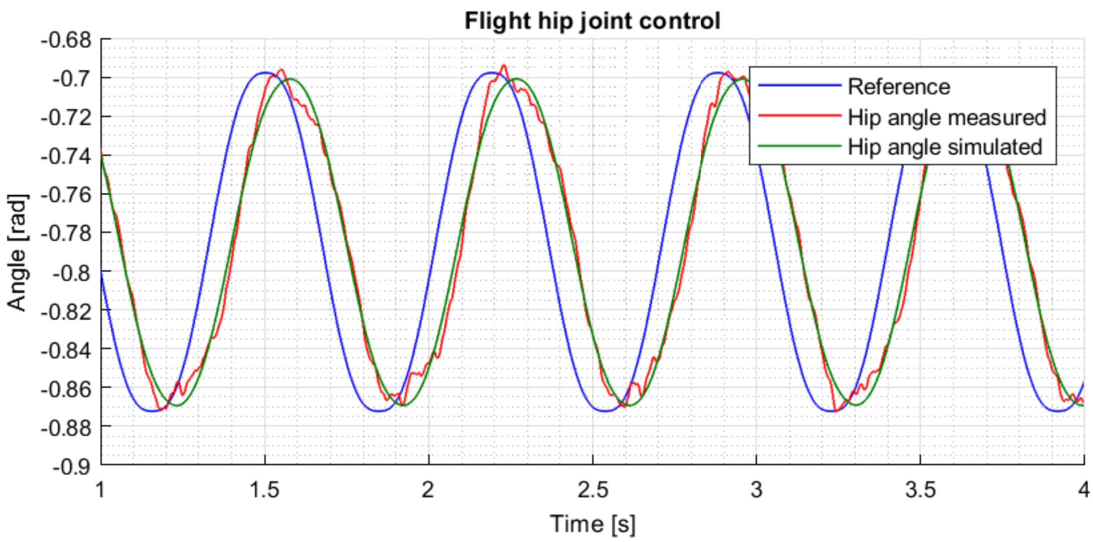

Figure 6.2: Upperleg flight phase response

6.1.2 Stance phase

For the stance phase tests, the leg is let to slide freely on the linear guide. The two controllers have to be tuned at the same time since the non-slipping condition on the two joint velocities derived in chapter 4 has to be maintained.

Lowerleg

As for the flight phase, the input reference has to be computed by subtracting from the spline signal the hip angle θ_1. The requested reference is the same for the fight test, with an amplitude of about 20 deg and a frequency around $1.43Hz$. The controller zero is increased till the system response becomes comparable to the simulation one, the final controller function is:

$$G_{c,ll,f}(s) = \frac{2.5(s+3)}{1+\dfrac{s}{50}} \tag{6.3}$$

The measured response is compared with the simulation one in Figure 6.3.

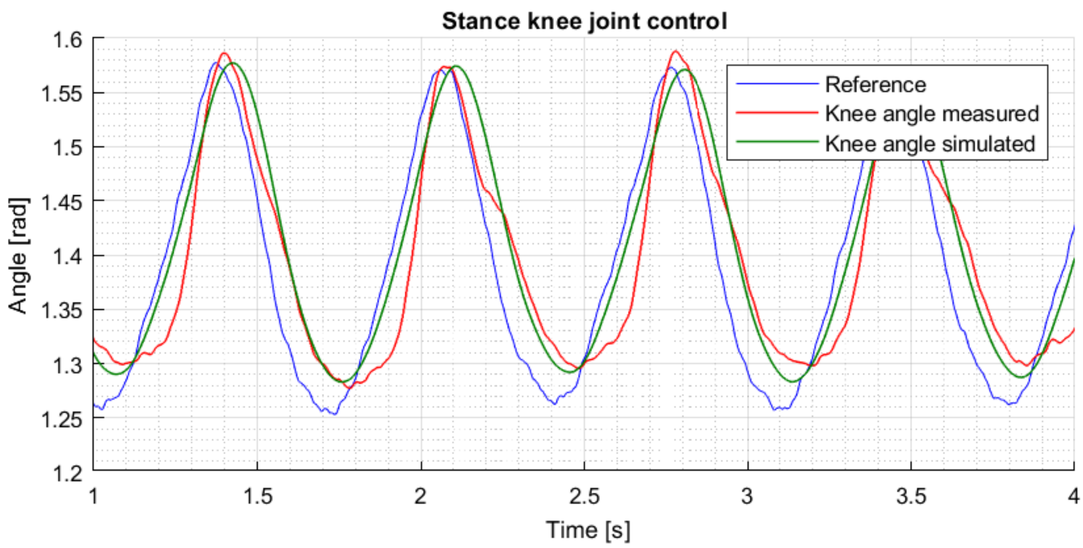

Figure 6.3: Lowerleg stance phase response

Upperleg

As for the flight phase, the input reference is directly computed with the spline signal. Its amplitude is about 10 deg, half with respect to the lowerleg one in order to keep the linearisation condition used during the mathematical model derivation in chapter 4. The signal frequency is kept, as for the lowerleg, around $1.43Hz$. The controller zero is increased till the system response becomes comparable to the simulation one, the final controller function is:

$$G_{c,ll,f}(s) = \frac{2.6(s+6)}{1+\dfrac{s}{40}} \tag{6.4}$$

The measured response is compared with the simulation one in Figure 6.4.

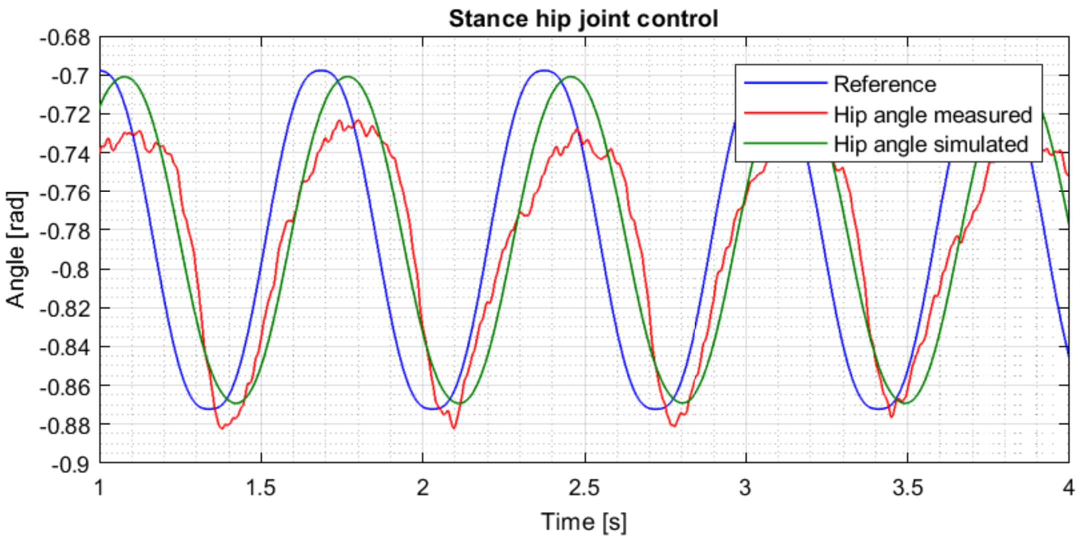

Figure 6.4: Upperleg stance phase response

6.2 Jump planning

One of the main aspects of this work is to show that the introduction of flexible link in the robot design can be an effective solution to reduce the energy consumption. The efficiency of the system can be increased defining a joint trajectory planning able to exploit the resonance phenomenon of the elastic element when the leg is in contact with the ground.
This phenomenon is also found in nature, in fact, when bipeds want to perform a sequence of jump, during the stance phase they have to squat down and then, thanks to a counter movement, they are able to lift off. As for bipeds to obtain a jump it is necessary to perform the same type of movements. To take advantages from the elastic energy stored into the link it is necessary to excite the flexible link at the resonance frequency.
The natural frequency of the system depends on the joint configuration, but, working in the range of angles defined in chapter 4, it is possible to assume that it is constant.
Due to the slowness of the designed controller, it is not possible to exploit the resonance of the flexible link to store the landing energy and to use it for the next jump. Moreover, the tendons broke during the first stance phase tests next to the thread drain groove, the smallest section along the bar, since it is still smaller than the re-dimensioned one because the terminators can't be substituted. This means that the prototype, in the current configuration, can not jump.
To help the leg to rise from the ground and to reduce a little the tendons stresses, a weight of $5kg$ is hanged to a pulley and linked to the support plate with a cable.

Since the system is changed, both the gravity compensator and the controller used for the stance phase has to be modified. Following the same procedure stated in section 5.1, the new gravity compensator for the stance phase is computed.

$$\begin{aligned} T_{hip} &= -10.87\sin(\theta_{hip}) \\ T_{knee} &= -14.53\sin(\theta_{hip}+\theta_{knee}) \end{aligned} \tag{6.5}$$

Through the computation of the new system mathematical models and the control law design process, it comes out that the change of support plate mass affects the control laws as a slight reduction of gain in order to keep the same loop shape unchanged.

The current state, flight or stance, at the beginning, was been derived from the strain gauge measurements. When the flexible link tip deformation was sensed to change suddenly, starting from the unloaded position, the transition from flight phase to stance was detected. Instead, if the flexible link tip deformation becomes negative, the detachment from the ground was detected. The main problem of this method came out from the signal conditioner shield, it wasn't stable enough on the strain gauge port. At each leg hit with the ground after a jump the calibration trimmer slightly moves changing the bridge output voltage making the unloaded condition unknown jump after jump. Then, for the state measurement, the knee torque sensor is used, since its signal conditioner port is more stable. The sensing logic is similar to the strain one. If suddenly the torque increases from the unloaded condition, the landing occurrence is detected, and if the measured torque lowers the unloaded one, the transition from stance phase to flight is detected.

To reduce the oscillation induced by the control action, it is necessary to use as reference signal a sufficiently smooth function. In this work a 5^{th} order polynomial trajectory is used because it allows to compute the trajectory between two points imposing also the initial and final velocities and accelerations.
Therefore, the squat movement reference for the hip joint is planned as a 5^{th} order polynomial trajectory with null initial and final accelerations, initial and final velocities opposite and with magnitude equal to $0.75rad/s$, and initial and final angles equal to $-\dfrac{\pi}{6}$. The duration, as shown in Figure 6.5, is of $0.4s$.

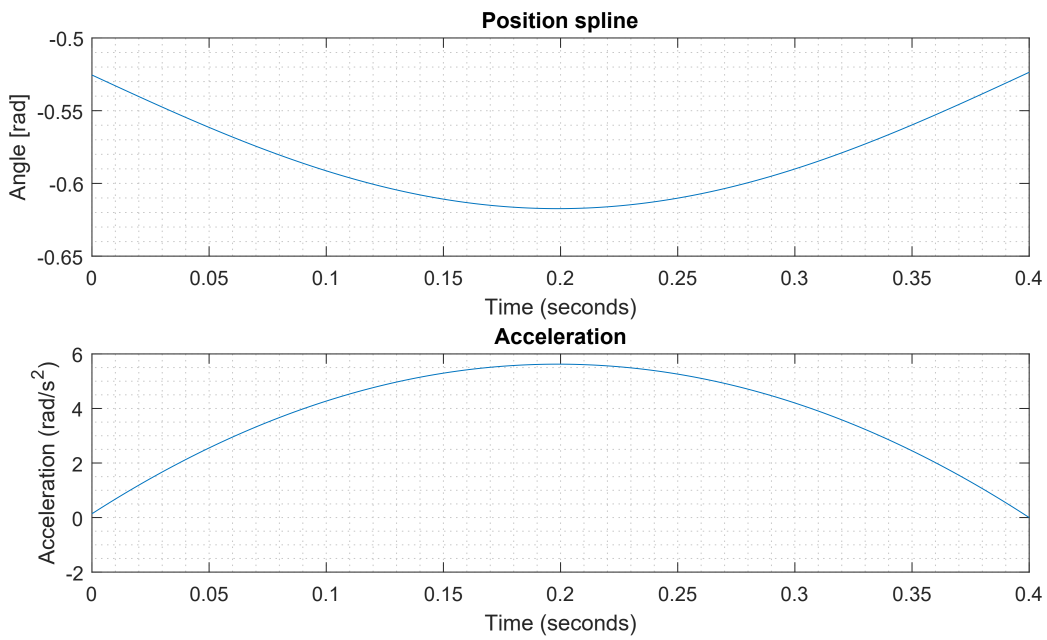

Figure 6.5: Hip joint trajectory

As stated in chapter 4, in equation 4.18, for the linearising condition, a fixed joint velocities relation has to be maintained: $\dot{\theta}_2 = -2\dot{\theta}_1$. Moreover, to keep the leg tip touch the ground under the hip joint, as derived again in chapter 4, in equation 4.16, there is a fixed relation between the hip and knee joint angles: $\theta_2 = -2\theta_1$.

Therefore, the squat movement reference for the hip joint is planned as a 5^{th} order polynomial trajectory with null initial and final accelerations, initial and final velocities opposite and with magnitude double with respect to the hip one, equal to $1.5rad/s$, and initial and final angles equal to the opposite and double with respect to the hip one, $\frac{\pi}{3}$. The duration, as shown in Figure 6.6, is of $0.4s$.

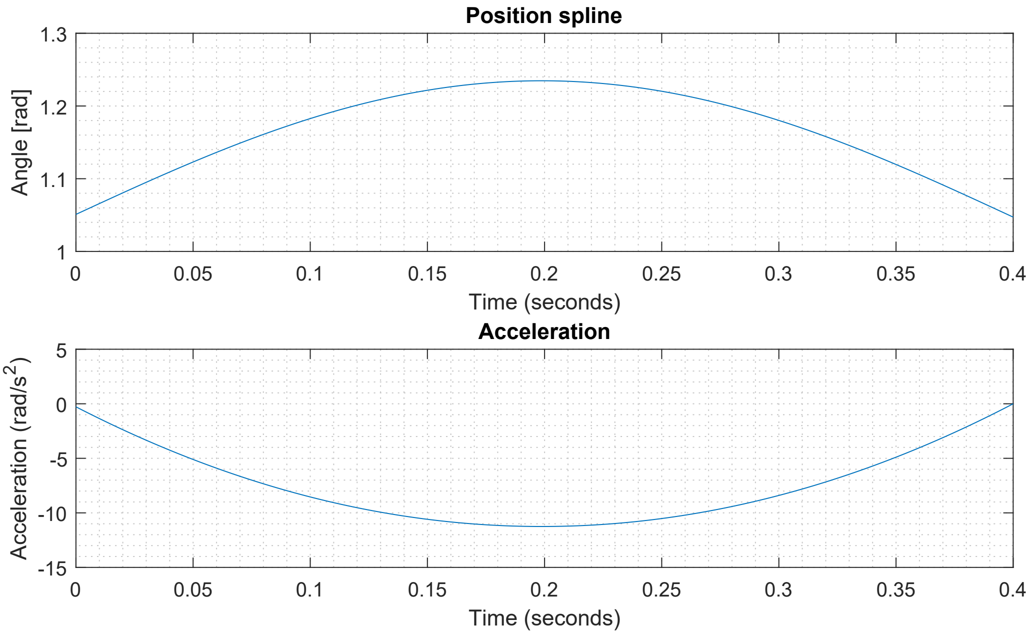

Figure 6.6: Knee joint trajectory

When the leg detaches from ground, two new 5^{th} order splines with null initial and final velocities and accelerations are computed as reference trajectories. The start angle is the current one and the final angle is the landing one: $\frac{\pi}{6}$ for the hip joint and $\frac{\pi}{3}$ for the knee one. The movement duration is set to be half the squat period, $T = 0.2s$.

The trajectory planning for making the leg jump is summarised in the flow chart shown in Figure 6.7.

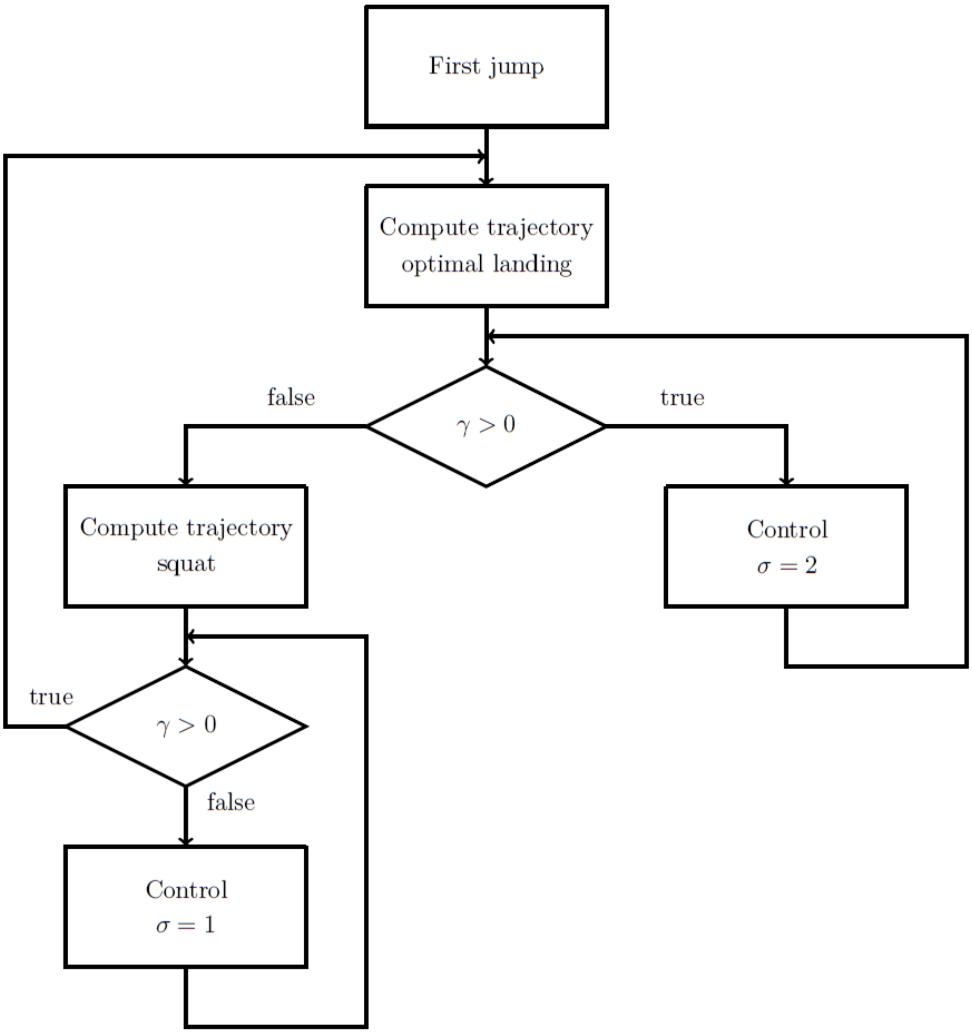

Figure 6.7: Trajectory planning flow chart

Finally, though not exploiting the resonance phenomenon, thanks to the hanged weight that unloaded the structure from too high stresses and compensated a little for the low worm-gear system efficiency, the leg is able to perform little jumps.

Chapter 7

Conclusions

Nowadays structural flexibility in robotics is often considered as a phenomenon to avoid. However, the introduction of elastic components could bring to safer and energy efficient mechanisms.
To analyze the benefits and the drawbacks introduced by the structural flexibility in robotic systems, a test rig has been used composed by an already-made two links robotic leg with one of them conceived as flexible. The goal of this work is to design a suitable controller for its actuation, as a first step in designing a new concept of a jumping humanoid robot as well as industrial robots.

In the first part of this work, an accurate characterization of the prototype is made in order to either measure or estimate all its electro-mechanical properties. The main goal of this process is to acquire all the data necessary for the computation of a model of the leg that can be used during the control design phase.
The analysis of the FlegX starts from the lowerleg subsystem. First, the tendons are re-dimensioned since they were subject to the buckling effect. Then, the flexible link is studied along with the strain gauge placed upon it devoted to the measurements of its deformation, both in statics and in dynamics: the sensor characteristics and the link natural frequencies and modal shapes are analyzed. The sensor characteristic is computed following tree different methods and the obtained results are compared in Figure 3.13. Further, the flexible link dynamical properties are derived through the Fourier analysis and the obtained results are compared with the FEM analysis results preformed during the mechanical design phase in Table 3.3. Then, the knee and hip torque sensors are analyzed. The simplest model is a linear characteristic, but, since the two sensors are affected by hysteresis, also a more accurate model is derived. The results are summarised in Figures 3.23 and 3.26. After, the mechanical properties like masses, inertias around the two revolute joints and bearings friction are either measured or estimated through the physical pendulum approach. Last, the two encoders are analyzed and, since they are too noisy to be used in a control loop, a suitable filter is designed. Some angle acquisitions and the relative filtering action are shown in Figure 3.32.
The only physical dimension that has not been possible to measure is the worm-gear system friction. Its contribution to the control action is studied starting from the mathematical model to its compensation achieved with the experimental controller tuning.

Once all the needed electro-mechanical properties are computed, a mathematical model of the leg is derived. Under the assumptions that the joint velocity is slow and that the mass is concentrated mostly on the linear guide, neglecting the gravity force that can be compensated in feed-forward, the equations describing the leg dynamics can be decoupled. Furthermore, the leg is analyzed into two different conditions: when it is both in flight phase and in stance phase. This brings to the definition of four different models, two for each subsystem. The four equations are derived through the Bond Graph approach by taking into account the uncertainty on the friction parameter. The resulting models are stated in equations (4.7), (4.12), (4.30) and (4.35). Finally, in order to derive the closed loop model for the control design phase, the motor model is derived through system identification.

Describing the dynamics of the leg through a hybrid dynamic system model, it is evident that it is necessary to design four different controllers, one for each state of each actuated subsystem. The proposed controller is based on a phase-lead network with a feed-forward term used to compensate the gravity effect. The scheme of the controlled closed loop system is shown in Figure 5.2.
The gravity compensation function is computed for both the flight and stance phases by deriving the joint torques needed for balancing the weight force. The obtained results are stated in equations (5.5) and (5.8).
Then, the phase-lead controllers are designed through the loop shaping technique by taking into account the friction uncertainty and analysing its contribution on the controller parameters. To keep the loop shape unchanged with an increase of the friction parameter, the zero of the controllers has to be increased. This leads to have only one degree of freedom. The controllers are then tuned experimentally and the obtained results are discussed in chapter 6 along with the jump trajectory planning.

One of the main merits of this work is to show that the introduction of flexible link in the robot design can be an effective solution to reduce the energy consumption. The efficiency of the system can be increased defining a joint trajectory planning able to exploit the resonance phenomenon of the elastic element when the leg is in contact with the ground. However, due to the encoder signals that need a filtering action and their low output signal frequency, the final controllers are not able to move the leg fast enough to evaluate the proposed phenomenon.
Moreover, during the experimental tests different mechanical critical issues arose, e.g. the tendons' break.
Anyhow, without the balancing hanged weight, the leg could not jump because of the low efficiency of the worm-gear system.
In order to carry out this work the mechanical structure has to be re-designed. New simulations on different structures are already in process. Also the sensors and the electronic shields have to be changed, faster and more reliable components are necessary to properly actuate the leg.

Then, studies about the modelling and control of flexible link structure can be carried on in order to take into account the link deformation and to be able to control the vibrations. With such a controller it is possible to reduce the settling time of the robot and to increase the positioning precision. This can bring to the design of a new concept of lightweight manipulators that are energy efficient and safer in terms of human robot interaction.
Lightweight robots can collaborate with people without hurting them in case of collisions, this means that in factories they have no need to be confined into cages without reducing

drastically their speed. Furthermore, they can be used for inspection purposes without the problem of damaging the surrounding environment. Flexible manipulators can also be used to handle fragile objects without spoiling them.

Appendices

Appendix A

Instrumentation used

Note: the pictures of the instruments are taken from the producer website.

Oscilloscope

Producer: Tektronix
Model: MSO2024B

Figure A.1: Oscilloscope Tektronix MSO2024B

Laser displacement sensor

Producer: Micro-Epsilon
Model: optoNCDT 1300-100

Figure A.2: Laser displacement sensor Micro-Epsilon optoNCDT 1300-100

Accelerometer

Producer: DYTRAN instruments, INC.
Model: 3255A2

Figure A.3: Accelerometer DYTRAN instruments, INC. 3255A2

Impact hammer

Producer: PCB PIEZOTRONICS
Model: 086C03

Figure A.4: Impact hammer PCB PIEZOTRONICS 086C03

Sensor signal conditioner

Producer: PCB PIEZOTRONICS
Model:482C series

Figure A.5: Impact hammer signal conditioner PCB PIEZOTRONICS 482C series

Load cell

Producer: burster
Model: 8417

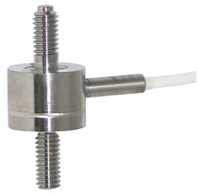

Figure A.6: Load cell burster 8417

Signal conditioner

Producer: burster
Model: 9235

Figure A.7: Load cell signal conditioner burster 9235

Bench scale

Producer: KERN
Model: FCB 6K0.5

Figure A.8: Bench scale KERN FCB 6K0.5

Hanging scale

Producer: KERN
Model: CH 50K50

Figure A.9: Hanging scale KERN CH 50K50

Bibliography

[1] Wallén, Johanna, "The History of the Industrial Robot", *Linköping University Electronic Press, 2008*

[2] Pratt, Jerry, and Gill Pratt. "Intuitive control of a planar bipedal walking robot." *ICRA*. 1998.

[3] Hester, Matthew S. "Stable control of jumping in a planar biped robot". *Diss.* The Ohio State University, 2009.

[4] Kim Donghyun, Zhao Ye, Thomas Gray, Sentis Luis. (2014). "Empirical Modifications To a Phase Space Planner Which Compensate For Low Stiffness Actuation in a Planar, Point-Foot, Biped Robot", *Conference: Proceedings of the ASME 2014 Dynamic Systems and Control Conference*

[5] Y. Hu, F. Nori and K. Mombaur, "Squat motion generation for the humanoid robot iCub with Series Elastic Actuators," *2016 6th IEEE International Conference on Biomedical Robotics and Biomechatronics (BioRob)*, Singapore, 2016, pp. 207-212.

[6] Hu Yue, Eljaik Jorhabib, Stein Kevin, Nori Francesco, Mombaur Katja. (2016). "Walking of the iCub humanoid robot in different scenarios: Implementation and performance analysis."

[7] J. Reher, E. A. Cousineau, A. Hereid, C. M. Hubicki and A. D. Ames, "Realizing dynamic and efficient bipedal locomotion on the humanoid robot DURUS," *2016 IEEE International Conference on Robotics and Automation (ICRA)*, Stockholm, 2016, pp. 1794-1801.

[8] Park, Jongwon, et al. "Raptor: Fast bipedal running and active tail stabilization." *Ubiquitous Robots and Ambient Intelligence (URAI)*, 2014 11th International Conference on. IEEE, 2014.

[9] D. W. Haldane, J. K. Yim and R. S. Fearing, "Repetitive extreme-acceleration (14-g) spatial jumping with Salto-1P," *2017 IEEE/RSJ International Conference on Intelligent Robots and Systems (IROS)*, Vancouver, BC, 2017, pp. 3345-3351.

[10] Niiyama, Ryuma, Satoshi Nishikawa, and Yasuo Kuniyoshi. "Biomechanical approach to open-loop bipedal running with a musculoskeletal athlete robot." *Advanced Robotics* 26.3-4 (2012)

[11] M. D'Imperio, D. Ludovico, C. Pizzamiglio, C. Canali, D. Caldwell and F. Cannella, "FLEGX: A bioinspired design for a jumping humanoid leg," *2017 IEEE/RSJ International Conference on Intelligent Robots and Systems (IROS)*, Vancouver, BC, 2017, pp. 3977-3982.

[12] D'Imperio M., Pizzamiglio C., Ludovico D., Caldwell D.G., Genta G., Cannella F. (2018) "Advanced Modelling Techniques for Flexible Robotic Systems." In: *Ferraresi C., Quaglia G. (eds) Advances in Service and Industrial Robotics. RAAD 2017.* Mechanisms and Machine Science, vol 49. Springer, Cham.

[13] M. D'Imperio, C. Pizzamiglio, D. Ludovico,L. Mentrasti, C. Canali, D. G. Caldwell and F. Cannella, "Towards Multi-Body Analyses for Advanced Flexible Robotic Systems". *ASME. International Design Engineering Technical Conferences and Computers and Information in Engineering Conference*, Volume 9.

[14] M. D'Imperio, D. Ludovico, C. Pizzamiglio,L. Mentrasti, D. G. Caldwell and F. Cannella, "FLEGX: Multibody Approach In Flexible Structure Design And Control." In:*ECCOMAS Thematic Conference on Multibody Dynamics June 19-22, 2017*, Prague, Czech Republic

[15] WF Stokey, "Vibration of systems having distributed mass and elasticity", In: *Shock and vibration Handbook, 1988, chapter 7*

[16] A.F. Bower, Brown University, *Free vibration of a damped, single degree of freedom, linear spring mass system*, Introduction to Dynamics and Vibrations, http://www.brown.edu

[17] D. Ludovico , M. D'Imperio and F. Cannella, "FLEGX: A Jumping Flexible Robotic Leg", In: *ASME, International Design Engineering Technical Conferences and Computers and Information in Engineering Conference, Volume 6 13th International Conference on Multibody Systems, Nonlinear Dynamics, and Control*

[18] J. Lygeros, C. Tomlin, and S. Sastry, "Hybrid systems: modeling, analysis and control," preprint, 1999.

[19] M.W.L.M. Rijnen, A.T. van Rijn, H. Dallali, A. Saccon and H. Nijmeijer, *Hybrid Trajectory Tracking for a Hopping Robotic Leg*, IFAC-PapersOnLine, Volume 49, **14**, (2016), 107–112